

MIT Open Access Articles

Amplitude analysis of $B^0 \rightarrow K^+ \pi^- \pi^0$ [$B^0 \rightarrow K^+ \pi^- \pi^0$ + $\pi^+ \pi^- \pi^0$] and evidence of direct CP violation in $B \rightarrow K^ \pi$ [$B \rightarrow K^* \pi$] decays*

The MIT Faculty has made this article openly available. **Please share** how this access benefits you. Your story matters.

Citation: Lees, J. P. et al. "Amplitude analysis of $B^0 \rightarrow K^+ \pi^- \pi^0$ and evidence of direct CP violation in $B \rightarrow K^* \pi$ decays" Phys. Rev. D 83, 112010 (2011). © 2011 American Physical Society

As Published: <http://dx.doi.org/10.1103/PhysRevD.83.112010>

Publisher: American Physical Society

Persistent URL: <http://hdl.handle.net/1721.1/65571>

Version: Final published version: final published article, as it appeared in a journal, conference proceedings, or other formally published context

Terms of Use: Article is made available in accordance with the publisher's policy and may be subject to US copyright law. Please refer to the publisher's site for terms of use.



Amplitude analysis of $B^0 \rightarrow K^+ \pi^- \pi^0$ and evidence of direct CP violation in $B \rightarrow K^* \pi$ decays

J. P. Lees,¹ V. Poireau,¹ E. Prencipe,¹ V. Tisserand,¹ J. Garra Tico,² E. Grauges,² M. Martinelli,^{3a,3b} D. A. Milanese,^{3a} A. Palano,^{3a,3b} M. Pappagallo,^{3a,3b} G. Eigen,⁴ B. Stugu,⁴ L. Sun,⁴ D. N. Brown,⁵ L. T. Kerth,⁵ Yu. G. Kolomensky,⁵ G. Lynch,⁵ H. Koch,⁶ T. Schroeder,⁶ D. J. Asgeirsson,⁷ C. Hearty,⁷ T. S. Mattison,⁷ J. A. McKenna,⁷ A. Khan,⁸ V. E. Blinov,⁹ A. R. Buzykaev,⁹ V. P. Druzhinin,⁹ V. B. Golubev,⁹ E. A. Kravchenko,⁹ A. P. Onuchin,⁹ S. I. Serednyakov,⁹ Yu. I. Skovpen,⁹ E. P. Solodov,⁹ K. Yu. Todyshev,⁹ A. N. Yushkov,⁹ M. Bondioli,¹⁰ S. Curry,¹⁰ D. Kirkby,¹⁰ A. J. Lankford,¹⁰ M. Mandelkern,¹⁰ D. P. Stoker,¹⁰ H. Atmacan,¹¹ J. W. Gary,¹¹ F. Liu,¹¹ O. Long,¹¹ G. M. Vitug,¹¹ C. Campagnari,¹¹ T. M. Hong,¹² D. Kovalskyi,¹² J. D. Richman,¹² C. A. West,¹² A. M. Eisner,¹³ J. Kroseberg,¹³ W. S. Lockman,¹³ A. J. Martinez,¹³ T. Schalk,¹³ B. A. Schumm,¹³ A. Seiden,¹³ C. H. Cheng,¹⁴ D. A. Doll,¹⁴ B. Echenard,¹⁴ K. T. Flood,¹⁴ D. G. Hitlin,¹⁴ P. Ongmongkolkul,¹⁴ F. C. Porter,¹⁴ A. Y. Rakitin,¹⁴ R. Andreassen,¹⁵ M. S. Dubrovin,¹⁵ B. T. Meadows,¹⁵ M. D. Sokoloff,¹⁵ P. C. Bloom,¹⁶ W. T. Ford,¹⁶ A. Gaz,¹⁶ M. Nagel,¹⁶ U. Nauenberg,¹⁶ J. G. Smith,¹⁶ S. R. Wagner,¹⁶ R. Ayad,^{17,*} W. H. Toki,¹⁷ B. Spaan,¹⁸ M. J. Kobel,¹⁹ K. R. Schubert,¹⁹ R. Schwierz,¹⁹ D. Bernard,²⁰ M. Verderi,²⁰ P. J. Clark,²¹ S. Playfer,²¹ J. E. Watson,²¹ D. Bettoni,^{22a,22b} C. Bozzi,^{22a} R. Calabrese,^{22a,22b} G. Cibinetto,^{22a,22b} E. Fioravanti,^{22a,22b} I. Garzia,^{22a,22b} E. Luppi,^{22a,22b} M. Munerato,^{22a,22b} M. Negrini,^{22a,22b} L. Piemontese,^{22a} R. Baldini-Ferrolì,²³ A. Calcaterra,²³ R. de Sangro,²³ G. Finocchiaro,²³ M. Nicolaci,²³ S. Pacetti,²³ P. Patteri,²³ I. M. Peruzzi,^{23,†} M. Piccolo,²³ M. Rama,²³ A. Zallo,²³ R. Contri,^{24a,24b} E. Guido,^{24a,24b} M. Lo Vetere,^{24a,24b} M. R. Monge,^{24a,24b} S. Passaggio,^{24a} C. Patrignani,^{24a,24b} E. Robutti,^{24a} B. Bhuyan,²⁵ V. Prasad,²⁵ C. L. Lee,²⁶ M. Morii,²⁶ A. J. Edwards,²⁷ A. Adametz,²⁸ J. Marks,²⁸ U. Uwer,²⁸ F. U. Bernlochner,²⁹ M. Ebert,²⁹ H. M. Lacker,²⁹ T. Lueck,²⁹ P. D. Dauncey,³⁰ M. Tibbetts,³⁰ P. K. Behera,³¹ U. Mallik,³¹ C. Chen,³² J. Cochran,³² H. B. Crawley,³² W. T. Meyer,³² S. Prell,³² E. I. Rosenberg,³² A. E. Rubin,³² A. V. Gritsan,³³ Z. J. Guo,³³ N. Arnaud,³⁴ M. Davier,³⁴ D. Derkach,³⁴ G. Grosdidier,³⁴ F. Le Diberder,³⁴ A. M. Lutz,³⁴ B. Malaescu,³⁴ P. Roudeau,³⁴ M. H. Schune,³⁴ A. Stocchi,³⁴ G. Wormser,³⁴ D. J. Lange,³⁵ D. M. Wright,³⁵ I. Bingham,³⁶ C. A. Chavez,³⁶ J. P. Coleman,³⁶ J. R. Fry,³⁶ E. Gabathuler,³⁶ D. E. Hutchcroft,³⁶ D. J. Payne,³⁶ C. Touramanis,³⁶ A. J. Bevan,³⁷ F. Di Lodovico,³⁷ R. Sacco,³⁷ M. Sigamani,³⁷ G. Cowan,³⁸ S. Paramesvaran,³⁸ D. N. Brown,³⁹ C. L. Davis,³⁹ A. G. Denig,⁴⁰ M. Fritsch,⁴⁰ W. Gradl,⁴⁰ A. Hafner,⁴⁰ K. E. Alwyn,⁴¹ D. Bailey,⁴¹ R. J. Barlow,⁴¹ G. Jackson,⁴¹ G. D. Lafferty,⁴¹ R. Cenci,⁴² B. Hamilton,⁴² A. Jawahery,⁴² D. A. Roberts,⁴² G. Simi,⁴² C. Dallapiccola,⁴³ E. Salvati,⁴³ R. Cowan,⁴⁴ D. Dujmic,⁴⁴ G. Sciolla,⁴⁴ D. Lindemann,⁴⁵ P. M. Patel,⁴⁵ S. H. Robertson,⁴⁵ M. Schram,⁴⁵ P. Biassoni,^{46a,46b} A. Lazzaro,^{46a,46b} V. Lombardo,^{46a} F. Palombo,^{46a,46b} S. Stracka,^{46a,46b} L. Cremaldi,⁴⁷ R. Godang,^{47,‡} R. Kroeger,⁴⁷ P. Sonnek,⁴⁷ D. J. Summers,⁴⁷ X. Nguyen,⁴⁸ P. Taras,⁴⁸ G. De Nardo,^{49a,49b} D. Monorchio,^{49a,49b} G. Onorato,^{49a,49b} C. Sciacca,^{49a,49b} G. Raven,⁵⁰ H. L. Snoek,⁵⁰ C. P. Jessop,⁵¹ K. J. Knoepfel,⁵¹ J. M. LoSecco,⁵¹ W. F. Wang,⁵¹ K. Honscheid,⁵² R. Kass,⁵² J. Brau,⁵³ R. Frey,⁵³ N. B. Sinev,⁵³ D. Strom,⁵³ E. Torrence,⁵³ E. Feltresi,^{54a,54b} N. Gagliardi,^{54a,54b} M. Margoni,^{54a,54b} M. Morandin,^{54a} M. Posocco,^{54a} M. Rotondo,^{54a} F. Simonetto,^{54a,54b} R. Stroili,^{54a,54b} E. Ben-Haim,⁵⁵ M. Bomben,⁵⁵ G. R. Bonneaud,⁵⁵ H. Briand,⁵⁵ G. Calderini,⁵⁵ J. Chauveau,⁵⁵ O. Hamon,⁵⁵ Ph. Leruste,⁵⁵ G. Marchiori,⁵⁵ J. Ocariz,⁵⁵ S. Sitt,⁵⁵ M. Biasini,^{56a,56b} E. Manoni,^{56a,56b} A. Rossi,^{56a,56b} C. Angelini,^{57a,57b} G. Batignani,^{57a,57b} S. Bettarini,^{57a,57b} M. Carpinelli,^{57a,57b,§} G. Casarosa,^{57a,57b} A. Cervelli,^{57a,57b} F. Forti,^{57a,57b} M. A. Giorgi,^{57a,57b} A. Lusiani,^{57a,57c} N. Neri,^{57a,57b} B. Oberhof,^{57a,57b} E. Paoloni,^{57a,57b} A. Perez,^{57a} G. Rizzo,^{57a,57b} J. J. Walsh,^{57a} D. Lopes Pegna,⁵⁸ C. Lu,⁵⁸ J. Olsen,⁵⁸ A. J. S. Smith,⁵⁸ A. V. Telnov,⁵⁸ F. Anulli,^{59a} G. Cavoto,^{59a} R. Faccini,^{59a,59b} F. Ferrarotto,^{59a} F. Ferroni,^{59a,59b} M. Gaspero,^{59a,59b} L. Li Gioi,^{59a} M. A. Mazzoni,^{59a} G. Piredda,^{59a} C. Büniger,⁶⁰ T. Hartmann,⁶⁰ T. Leddig,⁶⁰ H. Schröder,⁶⁰ R. Waldi,⁶⁰ T. Adye,⁶¹ E. O. Olaiya,⁶¹ F. F. Wilson,⁶¹ S. Emery,⁶² G. Hamel de Monchenault,⁶² G. Vasseur,⁶² Ch. Yèche,⁶² D. Aston,⁶³ D. J. Bard,⁶³ R. Bartoldus,⁶³ J. F. Benitez,⁶³ C. Cartaro,⁶³ M. R. Convery,⁶³ J. Dorfan,⁶³ G. P. Dubois-Felsmann,⁶³ W. Dunwoodie,⁶³ R. C. Field,⁶³ M. Franco Sevilla,⁶³ B. G. Fulsom,⁶³ A. M. Gabareen,⁶³ M. T. Graham,⁶³ P. Grenier,⁶³ C. Hast,⁶³ W. R. Innes,⁶³ M. H. Kelsey,⁶³ H. Kim,⁶³ P. Kim,⁶³ M. L. Kocian,⁶³ D. W. G. S. Leith,⁶³ P. Lewis,⁶³ S. Li,⁶³ B. Lindquist,⁶³ S. Luitz,⁶³ V. Luth,⁶³ H. L. Lynch,⁶³ D. B. MacFarlane,⁶³ D. R. Muller,⁶³ H. Neal,⁶³ S. Nelson,⁶³ I. Ofte,⁶³ M. Perl,⁶³ T. Pulliam,⁶³ B. N. Ratcliff,⁶³ A. Roodman,⁶³ A. A. Salnikov,⁶³ V. Santoro,⁶³ R. H. Schindler,⁶³ A. Snyder,⁶³ D. Su,⁶³ M. K. Sullivan,⁶³ J. Va'vra,⁶³ A. P. Wagner,⁶³ M. Weaver,⁶³ W. J. Wisniewski,⁶³ M. Wittgen,⁶³ D. H. Wright,⁶³ H. W. Wulsin,⁶³ A. K. Yarritu,⁶³ C. C. Young,⁶³ V. Ziegler,⁶³ W. Park,⁶⁴ M. V. Purohit,⁶⁴ R. M. White,⁶⁴ J. R. Wilson,⁶⁴ A. Randle-Conde,⁶⁵ S. J. Sekula,⁶⁵ M. Bellis,⁶⁶ P. R. Burchat,⁶⁶ T. S. Miyashita,⁶⁶ M. S. Alam,⁶⁷ J. A. Ernst,⁶⁷ R. Gorodeisky,⁶⁸ N. Guttman,⁶⁸ D. R. Peimer,⁶⁸ A. Soffer,⁶⁸ P. Lund,⁶⁹ S. M. Spanier,⁶⁹ R. Eckmann,⁷⁰ J. L. Ritchie,⁷⁰ A. M. Ruland,⁷⁰ C. J. Schilling,⁷⁰ R. F. Schwitters,⁷⁰ B. C. Wray,⁷⁰ J. M. Izen,⁷¹ X. C. Lou,⁷¹ F. Bianchi,^{72a,72b} D. Gamba,^{72a,72b} L. Lancieri,^{73a,73b} L. Vitale,^{73a,73b} N. Lopez-March,⁷⁴ F. Martinez-Vidal,⁷⁴ A. Oyanguren,⁷⁴ H. Ahmed,⁷⁵

J. Albert,⁷⁵ Sw. Banerjee,⁷⁵ H. H. F. Choi,⁷⁵ G. J. King,⁷⁵ R. Kowalewski,⁷⁵ M. J. Lewczuk,⁷⁵ C. Lindsay,⁷⁵ I. M. Nugent,⁷⁵ J. M. Roney,⁷⁵ R. J. Sobie,⁷⁵ T. J. Gershon,⁷⁶ P. F. Harrison,⁷⁶ T. E. Latham,⁷⁶ E. M. T. Puccio,⁷⁶ H. R. Band,⁷⁷ S. Dasu,⁷⁷ Y. Pan,⁷⁷ R. Prepost,⁷⁷ C. O. Vuosalo,⁷⁷ and S. L. Wu⁷⁷

(BABAR Collaboration)

- ¹Laboratoire d'Annecy-le-Vieux de Physique des Particules (LAPP), Université de Savoie, CNRS/IN2P3, F-74941 Annecy-Le-Vieux, France
- ²Universitat de Barcelona, Facultat de Física, Departament ECM, E-08028 Barcelona, Spain
- ^{3a}INFN Sezione di Bari, I-70126 Bari, Italy
- ^{3b}Dipartimento di Fisica, Università di Bari, I-70126 Bari, Italy
- ⁴University of Bergen, Institute of Physics, N-5007 Bergen, Norway
- ⁵Lawrence Berkeley National Laboratory and University of California, Berkeley, California 94720, USA
- ⁶Ruhr Universität Bochum, Institut für Experimentalphysik I, D-44780 Bochum, Germany
- ⁷University of British Columbia, Vancouver, British Columbia, Canada V6T 1Z1
- ⁸Brunel University, Uxbridge, Middlesex UB8 3PH, United Kingdom
- ⁹Budker Institute of Nuclear Physics, Novosibirsk 630090, Russia
- ¹⁰University of California at Irvine, Irvine, California 92697, USA
- ¹¹University of California at Riverside, Riverside, California 92521, USA
- ¹²University of California at Santa Barbara, Santa Barbara, California 93106, USA
- ¹³University of California at Santa Cruz, Institute for Particle Physics, Santa Cruz, California 95064, USA
- ¹⁴California Institute of Technology, Pasadena, California 91125, USA
- ¹⁵University of Cincinnati, Cincinnati, Ohio 45221, USA
- ¹⁶University of Colorado, Boulder, Colorado 80309, USA
- ¹⁷Colorado State University, Fort Collins, Colorado 80523, USA
- ¹⁸Technische Universität Dortmund, Fakultät Physik, D-44221 Dortmund, Germany
- ¹⁹Technische Universität Dresden, Institut für Kern- und Teilchenphysik, D-01062 Dresden, Germany
- ²⁰Laboratoire Leprince-Ringuet, CNRS/IN2P3, Ecole Polytechnique, F-91128 Palaiseau, France
- ²¹University of Edinburgh, Edinburgh EH9 3JZ, United Kingdom
- ^{22a}INFN Sezione di Ferrara, I-44100 Ferrara, Italy
- ^{22b}Dipartimento di Fisica, Università di Ferrara, I-44100 Ferrara, Italy
- ²³INFN Laboratori Nazionali di Frascati, I-00044 Frascati, Italy
- ^{24a}INFN Sezione di Genova, I-16146 Genova, Italy
- ^{24b}Dipartimento di Fisica, Università di Genova, I-16146 Genova, Italy
- ²⁵Indian Institute of Technology Guwahati, Guwahati, Assam, 781 039, India
- ²⁶Harvard University, Cambridge, Massachusetts 02138, USA
- ²⁷Harvey Mudd College, Claremont, California 91711
- ²⁸Universität Heidelberg, Physikalisches Institut, Philosophenweg 12, D-69120 Heidelberg, Germany
- ²⁹Humboldt-Universität zu Berlin, Institut für Physik, Newtonstr. 15, D-12489 Berlin, Germany
- ³⁰Imperial College London, London, SW7 2AZ, United Kingdom
- ³¹University of Iowa, Iowa City, Iowa 52242, USA
- ³²Iowa State University, Ames, Iowa 50011-3160, USA
- ³³Johns Hopkins University, Baltimore, Maryland 21218, USA
- ³⁴Laboratoire de l'Accélérateur Linéaire, IN2P3/CNRS et Université Paris-Sud 11, Centre Scientifique d'Orsay, B. P. 34, F-91898 Orsay Cedex, France
- ³⁵Lawrence Livermore National Laboratory, Livermore, California 94550, USA
- ³⁶University of Liverpool, Liverpool L69 7ZE, United Kingdom
- ³⁷Queen Mary, University of London, London, E1 4NS, United Kingdom
- ³⁸University of London, Royal Holloway and Bedford New College, Egham, Surrey TW20 0EX, United Kingdom
- ³⁹University of Louisville, Louisville, Kentucky 40292, USA
- ⁴⁰Johannes Gutenberg-Universität Mainz, Institut für Kernphysik, D-55099 Mainz, Germany
- ⁴¹University of Manchester, Manchester M13 9PL, United Kingdom
- ⁴²University of Maryland, College Park, Maryland 20742, USA
- ⁴³University of Massachusetts, Amherst, Massachusetts 01003, USA
- ⁴⁴Massachusetts Institute of Technology, Laboratory for Nuclear Science, Cambridge, Massachusetts 02139, USA
- ⁴⁵McGill University, Montréal, Québec, Canada H3A 2T8
- ^{46a}INFN Sezione di Milano, I-20133 Milano, Italy
- ^{46b}Dipartimento di Fisica, Università di Milano, I-20133 Milano, Italy
- ⁴⁷University of Mississippi, University, Mississippi 38677, USA

- ⁴⁸*Université de Montréal, Physique des Particules, Montréal, Québec, Canada H3C 3J7*
^{49a}*INFN Sezione di Napoli, I-80126 Napoli, Italy*
^{49b}*Dipartimento di Scienze Fisiche, Università di Napoli Federico II, I-80126 Napoli, Italy*
⁵⁰*NIKHEF, National Institute for Nuclear Physics and High Energy Physics, NL-1009 DB Amsterdam, The Netherlands*
⁵¹*University of Notre Dame, Notre Dame, Indiana 46556, USA*
⁵²*Ohio State University, Columbus, Ohio 43210, USA*
⁵³*University of Oregon, Eugene, Oregon 97403, USA*
^{54a}*INFN Sezione di Padova, I-35131 Padova, Italy*
^{54b}*Dipartimento di Fisica, Università di Padova, I-35131 Padova, Italy*
⁵⁵*Laboratoire de Physique Nucléaire et de Hautes Energies, IN2P3/CNRS, Université Pierre et Marie Curie-Paris6, Université Denis Diderot-Paris7, F-75252 Paris, France*
^{56a}*INFN Sezione di Perugia, I-06100 Perugia, Italy*
^{56b}*Dipartimento di Fisica, Università di Perugia, I-06100 Perugia, Italy*
^{57a}*INFN Sezione di Pisa, I-56127 Pisa, Italy*
^{57b}*Dipartimento di Fisica, Università di Pisa, I-56127 Pisa, Italy*
^{57c}*Scuola Normale Superiore di Pisa, I-56127 Pisa, Italy*
⁵⁸*Princeton University, Princeton, New Jersey 08544, USA*
^{59a}*INFN Sezione di Roma, I-00185 Roma, Italy*
^{59b}*Dipartimento di Fisica, Università di Roma La Sapienza, I-00185 Roma, Italy*
⁶⁰*Universität Rostock, D-18051 Rostock, Germany*
⁶¹*Rutherford Appleton Laboratory, Chilton, Didcot, Oxon, OX11 0QX, United Kingdom*
⁶²*CEA, Irfu, SPP, Centre de Saclay, F-91191 Gif-sur-Yvette, France*
⁶³*SLAC National Accelerator Laboratory, Stanford, California 94309 USA*
⁶⁴*University of South Carolina, Columbia, South Carolina 29208, USA*
⁶⁵*Southern Methodist University, Dallas, Texas 75275, USA*
⁶⁶*Stanford University, Stanford, California 94305-4060, USA*
⁶⁷*State University of New York, Albany, New York 12222, USA*
⁶⁸*Tel Aviv University, School of Physics and Astronomy, Tel Aviv, 69978, Israel*
⁶⁹*University of Tennessee, Knoxville, Tennessee 37996, USA*
⁷⁰*University of Texas at Austin, Austin, Texas 78712, USA*
⁷¹*University of Texas at Dallas, Richardson, Texas 75083, USA*
^{72a}*INFN Sezione di Torino, I-10125 Torino, Italy*
^{72b}*Dipartimento di Fisica Sperimentale, Università di Torino, I-10125 Torino, Italy*
^{73a}*INFN Sezione di Trieste, I-34127 Trieste, Italy*
^{73b}*Dipartimento di Fisica, Università di Trieste, I-34127 Trieste, Italy*
⁷⁴*IFIC, Universitat de Valencia-CSIC, E-46071 Valencia, Spain*
⁷⁵*University of Victoria, Victoria, British Columbia, Canada V8W 3P6*
⁷⁶*Department of Physics, University of Warwick, Coventry CV4 7AL, United Kingdom*
⁷⁷*University of Wisconsin, Madison, Wisconsin 53706, USA*

(Received 1 May 2011; published 29 June 2011)

We analyze the decay $B^0 \rightarrow K^+ \pi^- \pi^0$ with a sample of $4.54 \times 10^8 B\bar{B}$ events collected by the BABAR detector at the PEP-II asymmetric-energy B factory at SLAC, and extract the complex amplitudes of seven interfering resonances over the Dalitz plot. These results are combined with amplitudes measured in $B^0 \rightarrow K_S^0 \pi^+ \pi^-$ decays to construct isospin amplitudes from $B^0 \rightarrow K^* \pi$ and $B^0 \rightarrow \rho K$ decays. We measure the phase of the isospin amplitude $\Phi_{3/2}$, useful in constraining the Cabibbo-Kobayashi-Maskawa unitarity triangle angle γ and evaluate a CP rate asymmetry sum rule sensitive to the presence of new physics operators. We measure direct CP violation in $B^0 \rightarrow K^{*+} \pi^-$ decays at the level of 3σ when measurements from both $B^0 \rightarrow K^+ \pi^- \pi^0$ and $B^0 \rightarrow K_S^0 \pi^+ \pi^-$ decays are combined.

DOI: 10.1103/PhysRevD.83.112010

PACS numbers: 11.30.Er, 11.30.Hv, 13.25.Hw

I. INTRODUCTION

In the standard model (SM), CP violation in weak interactions is parametrized by an irreducible complex phase in the Cabibbo-Kobayashi-Maskawa (CKM) quark mixing matrix [1,2]. The unitarity of the CKM matrix is typically expressed as a triangular relationship among its parameters such that decay amplitudes are sensitive to the

*Now at Temple University, Philadelphia, PA 19122, USA

†Also with Università di Perugia, Dipartimento di Fisica, Perugia, Italy

‡Now at University of South Alabama, Mobile, AL 36688, USA

§Also with Università di Sassari, Sassari, Italy

angles of the triangle denoted α , β , γ . Redundant measurements of the parameters of the CKM matrix provide an important test of the SM, since violation of the unitarity condition would be a signature of new physics. The angle γ remains the least well measured of the CKM angles. Tree amplitudes in $B \rightarrow K^* \pi$ decays are sensitive to γ but are Cabibbo-suppressed relative to loop-order (penguin) contributions involving radiation of either a gluon (QCD penguins) or a photon (electroweak penguins or EWPs) from the loop.

It has been shown that QCD penguin contributions can be eliminated by constructing a linear combination of $B^0 \rightarrow K^{*+} \pi^-$ and $B^0 \rightarrow K^{*0} \pi^0$ weak decay amplitudes that is pure (isospin) $I = 3/2$ [3],

$$\mathcal{A}_{3/2}(K^* \pi) = \frac{1}{\sqrt{2}} \mathcal{A}(B^0 \rightarrow K^{*+} \pi^-) + \mathcal{A}(B^0 \rightarrow K^{*0} \pi^0). \quad (1)$$

Since a transition from $I = \frac{1}{2}$ to $I = 3/2$ is possible only via $\Delta I = 1$ operators, $\mathcal{A}_{3/2}$ must be free of $\Delta I = 0$, namely, QCD contributions. The weak phase of $\mathcal{A}_{3/2}$, given by $\Phi_{3/2} = -\frac{1}{2} \text{Arg}(\bar{\mathcal{A}}_{3/2}/\mathcal{A}_{3/2})$, is equal to the CKM angle γ in the absence of EWP operators [4]. Here, $\bar{\mathcal{A}}_{3/2}$ denotes the CP conjugate of the amplitude in Eq. (1).

The relative magnitudes and phases of the $B^0 \rightarrow K^{*+} \pi^-$ and $B^0 \rightarrow K^{*0} \pi^0$ amplitudes in Eq. (1) are measured from their interference over the available decay phase space (Dalitz plot or DP) to the common final state $B^0 \rightarrow K^+ \pi^- \pi^0$. The phase difference between $B^0 \rightarrow K^{*+} \pi^-$ and $\bar{B}^0 \rightarrow K^{*-} \pi^+$ is measured in the DP analysis of the self-conjugate final state $B^0 \rightarrow K_S^0 \pi^+ \pi^-$ [5] where the strong phases cancel. This argument is extended to $B^0 \rightarrow \rho K$ decay amplitudes [6,7] where an isospin decomposition of amplitudes gives

$$\mathcal{A}_{3/2}(\rho K) = \frac{1}{\sqrt{2}} \mathcal{A}(B^0 \rightarrow \rho^- K^+) + \mathcal{A}(B^0 \rightarrow \rho^0 K^0). \quad (2)$$

Here, the $B^0 \rightarrow \rho^- K^+$ and $B^0 \rightarrow \rho^0 K^0$ decays do not decay to a common final state preventing a direct measurement of their relative phase. The amplitudes in Eq. (2) do, however, interfere with the $B^0 \rightarrow K^{*+} \pi^-$ amplitude in their decays to $B^0 \rightarrow K^+ \pi^- \pi^0$ and $B^0 \rightarrow K_S^0 \pi^+ \pi^-$ final states so that an indirect measurement of their relative phase is possible.

The CP rate asymmetries of the isospin amplitudes $\mathcal{A}_{3/2}(K^* \pi)$ and $\mathcal{A}_{3/2}(\rho K)$ have been shown to obey a sum rule [8],

$$|\bar{\mathcal{A}}_{3/2}(K^* \pi)|^2 - |\mathcal{A}_{3/2}(K^* \pi)|^2 = |\mathcal{A}_{3/2}(\rho K)|^2 - |\bar{\mathcal{A}}_{3/2}(\rho K)|^2. \quad (3)$$

This sum rule is exact in the limit of SU(3) symmetry and large deviations could be an indication of new strangeness violating operators. Measurements of

$B^0 \rightarrow K^* \pi$ and $B^0 \rightarrow \rho K$ amplitudes are used to evaluate Eq. (3).

We present an update of the DP analysis of the flavor-specific $B^0 \rightarrow K^+ \pi^- \pi^0$ decay from Ref. [9] with a sample of $4.54 \times 10^8 B\bar{B}$ events. The isobar model used to parametrize the complex amplitudes of the intermediate resonances contributing to the final state is presented in Sec. II. The BABAR detector and data set are briefly described in Sec. III. The efficient selection of signal candidates is described in Sec. IV and the unbinned maximum likelihood (ML) fit performed with the selected events is presented in Sec. V. The complex amplitudes of the intermediate resonances contributing to the $B^0 \rightarrow K^+ \pi^- \pi^0$ decay are extracted from the result of the ML fit in Sec. VI together with the accounting of the systematic uncertainties in Sec. VII. Several important results are discussed in Sec. VIII. Measurements of $B^0 \rightarrow \rho K$ from this article and Ref. [5] are used to produce a measurement of $\Phi_{3/2}$ using Eq. (2). It is shown that the large phase difference between $B^0 \rightarrow K^{*+}(892)\pi^-$ and $B^0 \rightarrow K^{*0}(892)\pi^0$ amplitudes makes a similar measurement using Eq. (1) impossible with the available data set. We find that the sum rule in Eq. (3) holds within the experimental uncertainty. Additionally, we find evidence for a direct CP asymmetry in $B^0 \rightarrow K^{*+} \pi^-$ decays when the results of Ref. [5] are combined with measurements in this article. The conventions and results of Ref. [5] are summarized where necessary. Finally in Sec. IX, we summarize our results.

II. ANALYSIS OVERVIEW

We present a DP analysis of the $B^0 \rightarrow K^+ \pi^- \pi^0$ decay in which we measure the magnitudes and relative phases of five resonant amplitudes: $\rho(770)^- K^+$, $\rho(1450)^- K^+$, $\rho(1700)^- K^+$, $K^*(892)^+ \pi^-$, $K^*(892)^0 \pi^0$, two $K\pi$ S-waves: $(K\pi)_0^{*0}$, $(K\pi)_0^{*+}$, and a nonresonant (NR) contribution, allowing for CP violation. The notation for the S-waves denotes phenomenological amplitudes described by coherent superpositions of an elastic effective-range term and the $K_0^*(1430)$ resonances [10]. Here, we describe the decay amplitude formalism and conventions used in this analysis.

The $B^0 \rightarrow K^+ \pi^- \pi^0$ decay amplitude is a function of two independent kinematic variables: we use the squares of the invariant masses of the pairs of particles $K^+ \pi^-$ and $K^+ \pi^0$, $x = m_{K^+ \pi^-}^2$ and $y = m_{K^+ \pi^0}^2$. The total decay amplitude is a linear combination of k isobars, each having amplitude \mathcal{A}_k given by

$$\mathcal{A}_k = a_k^{(-)} e^{i\Phi_k^{(-)}} \int_{\text{DP}} f_k(J, x, y) dx dy, \quad (4)$$

where

$$\left| \int_{\text{DP}} f_k(J, x, y) dx dy \right| = 1. \quad (5)$$

Here, $\bar{\mathcal{A}}_k$ denotes the CP conjugate amplitude and $a_k e^{i\Phi_k^{(-)}}$ is the complex coefficient of the isobar. The normalized decay dynamics of the intermediate state are specified by the functions f_k that for a spin- J resonance in the $K^+ \pi^-$ decay channel describe the angular dependence $T_k(J, x, y)$, Blatt-Weisskopf centrifugal barrier factor [11] $B_k(J, x)$, and mass distribution of the resonance $L_k(J, x)$,

$$f_k(J, x, y) = T_k(J, x, y) \times B_k(J, x) \times L_k(J, x). \quad (6)$$

The branching fractions \mathcal{B}_k (CP averaged over B^0 and \bar{B}^0), and CP asymmetry, $A_{CP}(k)$, are given by

$$\mathcal{B}_k = \frac{|\mathcal{A}_k|^2 + |\bar{\mathcal{A}}_k|^2}{\sum_j |\mathcal{A}_j|^2 + \sum_j |\bar{\mathcal{A}}_j|^2} \times \frac{N_{\text{sig}}}{N_{B\bar{B}} \langle \epsilon \rangle_{\text{DP}}}, \quad (7)$$

$$A_{CP}(k) = \frac{|\bar{\mathcal{A}}_k|^2 - |\mathcal{A}_k|^2}{|\bar{\mathcal{A}}_k|^2 + |\mathcal{A}_k|^2} = \frac{\bar{a}_k^2 - a_k^2}{\bar{a}_k^2 + a_k^2}, \quad (8)$$

where N_{sig} is the number of $B^0 \rightarrow K^+ \pi^- \pi^0$ events selected from a sample of $N_{B\bar{B}}$ B -meson decays. The average DP efficiency, $\langle \epsilon \rangle_{\text{DP}}$, is given by

$$\frac{|\sum_k (a_k e^{i\Phi_k} + \bar{a}_k e^{i\bar{\Phi}_k}) \int_{\text{DP}} \epsilon(x, y) f_k(J, x, y) dx dy|}{|\sum_k (a_k e^{i\Phi_k} + \bar{a}_k e^{i\bar{\Phi}_k}) \int_{\text{DP}} f_k(J, x, y) dx dy|}, \quad (9)$$

where $\epsilon(x, y)$ is the DP-dependent signal selection efficiency.

We use the Zemach tensor formalism [12] for the angular distribution $T(J, x, y)$ of a process by which a pseudoscalar B -meson produces a spin- J resonance in association with a bachelor pseudoscalar meson. We define \vec{p} and \vec{q} as the momentum vectors of the bachelor particle and resonance decay product, respectively, in the rest frame of the resonance k . The choice of the resonance decay product defines the helicity convention for each resonance where the cosine of the helicity angle is $\cos\theta_H = \vec{p} \cdot \vec{q} / (|\vec{p}||\vec{q}|)$. We choose the resonance decay product with momentum \vec{q} to be the π^- for $K^+ \pi^-$ resonances, the π^0 for $\pi^- \pi^0$ resonances, and the K^+ for $\pi^0 K^+$ resonances (see Fig. 1).

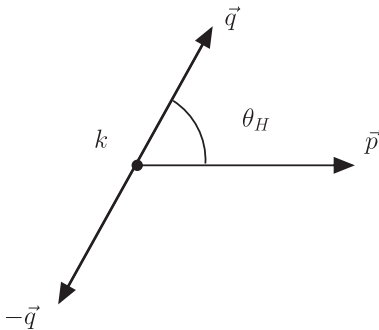


FIG. 1. The helicity angle (θ_H) and momenta of particles (\vec{q} , \vec{p}) in the rest frame of a resonance k .

TABLE I. The angular distributions $T(J, x, y)$, and Blatt-Weisskopf barrier factors $B(J, x)$, for a resonance of spin- J decaying to two pseudoscalar mesons.

Spin- J	$T(J, x, y)$	$B(J, x)$
0	1	1
1	$-2 \vec{p} \vec{q} \cos\theta_H$	$\sqrt{\frac{1+z_0^2}{1+z^2}}$
2	$\frac{4}{3} \vec{p} ^2 \vec{q} ^2(3\cos^2\theta_H - 1)$	$\sqrt{\frac{9+3z_0^2+z^2}{9+3z^2+z^4}}$

The decay of a spin- J resonance into two pseudoscalars is damped by a Blatt-Weisskopf barrier factor, characterized by the phenomenological radius R of the resonance. The Blatt-Weisskopf barrier factors $B(J, x)$ are normalized to 1 when \sqrt{x} equals the pole mass M of the resonance. We parametrize the barrier factors in terms of $z = |\vec{q}|R$ and $z_0 = |\vec{q}_0|R$, where $|\vec{q}_0|$ is the value of $|\vec{q}|$ when $\sqrt{x} = M$. The angular distributions and Blatt-Weisskopf barrier factors for the resonance spins used in this analysis are summarized in Table I.

We use the relativistic Breit-Wigner (RBW) line shape to describe the $K^*(892)^{+,0}$ resonances,

$$L^{\text{RBW}}(J, x) = \frac{1}{M^2 - x - iM\Gamma(J, x)}. \quad (10)$$

Here, the mass-dependent width $\Gamma(J, x)$ is defined by

$$\Gamma(J, x) = \Gamma^0 \frac{M}{\sqrt{x}} \left(\frac{|\vec{q}|}{|\vec{q}_0|} \right)^{2J+1} B(J, x)^2, \quad (11)$$

where Γ^0 is the natural width of the resonance.

The Gounaris-Sakurai (GS) parametrization [13] is used to describe the line shape of the broad $\rho(770)^-$, $\rho(1450)^-$ and $\rho(1700)^-$ resonances decaying to two pions,

$$L^{\text{GS}}(J, x) = \frac{1 + d\Gamma^0/M}{M^2 + g(x) - x - iM\Gamma(J, x)}, \quad (12)$$

where $\Gamma(J, x)$ is defined in Eq. (11). Expressions for the constant d and the function $g(x)$ in terms of M and Γ^0 are given in Ref. [13]. The parameters of the ρ line shapes, M , and Γ^0 are taken from Ref. [14] using updated line-shape fits with data from e^+e^- annihilation [15] and τ decays [16].

An effective-range parametrization was suggested [17] for the $K\pi$ scalar amplitudes, $(K\pi)_0^{*+}$ and $(K\pi)_0^{*0}$ which dominate for $m_{K\pi} < 2 \text{ GeV}/c^2$, to describe the slowly increasing phase as a function of the $K\pi$ mass. We use the parametrization chosen in the LASS experiment [18], tuned for B -meson decays [10],

$$L^{\text{LASS}}(x) = \frac{\sqrt{x}/M^2}{|\vec{q}|\cot\delta_B - i|\vec{q}|} + e^{2i\delta_B} \frac{\Gamma^0/|\vec{q}_0|}{M^2 - x - iM\Gamma(0, x)}, \quad (13)$$

with

$$\cot\delta_B = \frac{1}{a|\vec{q}|} + \frac{1}{2}r|\vec{q}|, \quad (14)$$

where a is the scattering length and r the effective range (see Table II). We impose a cutoff for the $K\pi$ S-waves so that L^{LASS} is given only by the second term in Eq. (13) for $\sqrt{x} > 1.8 \text{ GeV}/c^2$. Finally, the NR $K^+\pi^-\pi^0$ amplitude is taken to be constant across the DP.

In addition to the seven resonant amplitudes and the NR component described above we model the contributions to the $K^+\pi^-\pi^0$ final state from $B^0 \rightarrow \bar{D}^0\pi^0$ and $B^0 \rightarrow D^-K^+$ with a double Gaussian distribution given by

TABLE II. The model for the $B^0 \rightarrow K^+\pi^-\pi^0$ decay comprises a nonresonant (NR) amplitude and seven intermediate states listed below. The three line shapes are described in the text and the citations reference the parameters used in the fit. We use the same LASS parameters [18] for both neutral and charged $K\pi$ systems.

Resonance	Line shape	Parameters
Spin- $J = 1$		
$\rho(770)^-$	GS [14]	$M = 775.5 \pm 0.6 \text{ MeV}/c^2$ $\Gamma^0 = 148.2 \pm 0.8 \text{ MeV}$ $R = 0_{-0.0}^{+1.5} (\text{GeV}/c)^{-1}$
$\rho(1450)^-$	GS [14]	$M = 1409 \pm 12 \text{ MeV}/c^2$ $\Gamma^0 = 500 \pm 37 \text{ MeV}$ $R = 0_{-0.0}^{+1.5} (\text{GeV}/c)^{-1}$
$\rho(1700)^-$	GS [14]	$M = 1749 \pm 20 \text{ MeV}/c^2$ $\Gamma^0 = 235 \pm 60 \text{ MeV}$ $R = 0_{-0.0}^{+1.5} (\text{GeV}/c)^{-1}$
$K^*(892)^+$	RBW [19]	$M = 891.6 \pm 0.26 \text{ MeV}/c^2$ $\Gamma^0 = 50 \pm 0.9 \text{ MeV}$ $R = 3.4 \pm 0.7 (\text{GeV}/c)^{-1}$
$K^*(892)^0$	RBW [19]	$M = 896.1 \pm 0.27 \text{ MeV}/c^2$ $\Gamma^0 = 50.5 \pm 0.6 \text{ MeV}$ $R = 3.4 \pm 0.7 (\text{GeV}/c)^{-1}$
Spin- $J = 0$		
$(K\pi)_0^{*+}, (K\pi)_0^{*0}$	LASS [18]	$M = 1412 \pm 3 \text{ MeV}/c^2$ $\Gamma^0 = 294 \pm 6 \text{ MeV}$ $a = 2.07 \pm 0.10 (\text{GeV}/c)^{-1}$ $r = 3.32 \pm 0.34 (\text{GeV}/c)^{-1}$
NR	Constant	
Noninterfering components		
\bar{D}^0	DG	$M_1 = 1862.3 \text{ MeV}/c^2$ $\sigma_1 = 7.1 \text{ MeV}$ $M_2 = 1860.1 \text{ MeV}/c^2$ $\sigma_2 = 22.4 \text{ MeV}$ $f = 0.12$
D^-	DG	$M_1 = 1864.4 \text{ MeV}/c^2$ $\sigma_1 = 9.9 \text{ MeV}$ $M_2 = 1860.6 \text{ MeV}/c^2$ $\sigma_2 = 21.3 \text{ MeV}$ $f = 0.32$

$$L^{\text{DG}}(x) = \frac{1-f}{\sigma_1} \exp\left[-\frac{(M_1 - \sqrt{x})^2}{2\sigma_1^2}\right] + \frac{f}{\sigma_2} \exp\left[-\frac{(M_2 - \sqrt{x})^2}{2\sigma_2^2}\right]. \quad (15)$$

The fraction f is the relative weight of the two Gaussian distributions parametrized by the masses M_1, M_2 and widths σ_1, σ_2 . The D -mesons are modeled as noninterfering isobars and are distinct from the charmless signal events.

III. THE BABAR DETECTOR AND DATA SET

The data used in this analysis were collected with the BABAR detector at the PEP-II asymmetric energy e^+e^- storage rings between October 1999 and September 2007. This corresponds to an integrated luminosity of 413 fb^{-1} or approximately $N_{B\bar{B}} = 4.54 \pm 0.05 \times 10^8 B\bar{B}$ pairs taken on the peak of the $Y(4S)$ resonance (on resonance) and 41 fb^{-1} recorded at a center-of-mass (CM) energy 40 MeV below (off resonance).

A detailed description of the BABAR detector is given in Ref. [20]. Charged-particle trajectories are measured by a five-layer, double-sided silicon vertex tracker (SVT) and a 40-layer drift chamber (DCH) coaxial with a 1.5 T magnetic field. Charged-particle identification is achieved by combining the information from a ring-imaging Cherenkov device (DIRC) and the ionization energy loss (dE/dx) measurements from the DCH and SVT. Photons are detected, and their energies are measured in a CsI(Tl) electromagnetic calorimeter (EMC) inside the coil. Muon candidates are identified in the instrumented flux return of the solenoid. We use GEANT4-based [21] software to simulate the detector response and account for the varying beam and environmental conditions. Using this software, we generate signal and background Monte Carlo (MC) event samples in order to estimate the efficiencies and expected backgrounds in this analysis.

IV. EVENT SELECTION AND BACKGROUNDS

We reconstruct $B^0 \rightarrow K^+\pi^-\pi^0$ candidates from a π^0 candidate and pairs of oppositely charged tracks that are required to form a good quality vertex. The charged-particle candidates are required to have transverse momenta above $100 \text{ MeV}/c$ and at least 12 hits in the DCH. We use information from the tracking system, EMC, and DIRC to select charged tracks consistent with either a kaon or pion hypothesis. The π^0 candidate is built from a pair of photons, each with an energy greater than 50 MeV in the laboratory frame and a lateral energy deposition profile in the EMC consistent with that expected for an electromagnetic shower. The invariant mass of each π^0 candidate, m_{π^0} , must be within 3 times the associated mass error, $\sigma(m_{\pi^0})$, of the nominal π^0 mass $134.9766 \text{ MeV}/c^2$ [19]. We also require $|\cos\theta_{\pi^0}^*|$, the modulus of the cosine of the

angle between the decay photon and the π^0 momentum vector in π^0 rest frame, to be less than 0.95.

A B^0 -meson candidate is characterized kinematically by the energy-substituted mass $m_{ES} \equiv \sqrt{(s/2 + \mathbf{p}_i \cdot \mathbf{p}_B)^2/E_i^2 - p_B^2}$ and the energy difference $\Delta E \equiv E_B^* - \frac{1}{2}\sqrt{s}$, where (E_B, \mathbf{p}_B) and (E_i, \mathbf{p}_i) are the four-vectors of the B candidate and the initial electron-positron system in the lab frame, respectively. The asterisk denotes the $Y(4S)$ frame, and s is the square of the invariant mass of the electron-positron system. We require $5.2720 \text{ GeV}/c^2 < m_{ES} < 5.2875 \text{ GeV}/c^2$. To avoid a bias in the DP from the dependence on the π^0 energy of the resolution in ΔE , we introduce the dimensionless quantity

$$\Delta E' = \frac{\frac{\Delta E}{\sigma(\Delta E)} + m_0 + m_1 x + m_2 x^2 + m_3 x^3}{w_0 + w_1 x + w_2 x^2 + w_3 x^3}, \quad (16)$$

where $\sigma(\Delta E)$ is the per event ΔE error and the coefficients, m_i , w_i given in Table III, are determined from fits to signal MC in bins of $x = m_{K^+\pi^-}^2 - (\text{GeV}/c^2)^2$. We require $|\Delta E'| \leq 2.1$. Following the calculation of these kinematic variables, each of the B candidates is refitted with its mass constrained to the world average value of the B -meson mass [19] in order to improve the DP position resolution and ensure that candidates occupy the physical region of the DP.

Backgrounds arise primarily from random combinations in $e^+e^- \rightarrow q\bar{q}$ (continuum) events. To enhance discrimination between signal and continuum, we use a neural network (NN) [22] to combine five discriminating variables: the angles with respect to the beam axis of the B momentum and B thrust axis in the $Y(4S)$ frame, the zeroth and second order monomials $L_{0,2}$ of the energy flow about the B thrust axis, and $\Delta z/\sigma(\Delta z)$, the significance of the flight distance between the two B -mesons. The monomials are defined by $L_n = \sum_i p_i \times |\cos\theta_i|^n$, where θ_i is the angle with respect to the B thrust axis of the track or neutral cluster i and p_i is the magnitude of its momentum. The sum excludes the tracks and neutral clusters comprising the B candidate. All quantities are calculated in the $Y(4S)$ frame. The NN is trained using off-resonance data and simulated signal events, all of which passed the selection criteria. The final sample of signal candidates is selected

TABLE III. Fitted values of m_i and w_i which minimize correlations of $\Delta E'$ with the DP position. The m_i , w_i have units of $(\text{GeV}/c^2)^{-2i}$.

i	$m_i(\times 10^{-3})$	$w_i(\times 10^{-3})$
0	246.36	1055.09
1	-2.73	6.86
2	1.14	0.66
3	-0.05	-0.03

with a requirement on the NN output that retains 81% of the signal and rejects 90% of continuum events.

Approximately 17% of the signal MC events which have B candidates passing all selection criteria except that on m_{ES} , contain multiple B candidates. Since the continuum DP is modeled from the m_{ES} sideband ($5.200 \text{ GeV}/c^2 \leq m_{ES} \leq 5.272 \text{ GeV}/c^2$) of on-peak data, the m_{ES} requirement is not applied in selecting the best B candidate. We select the candidate with the minimum value of

$$\chi^2 = \left(\frac{m_{\pi^0} - 134.9766 \text{ GeV}/c^2}{\sigma(m_{\pi^0})} \right)^2 + \chi_{\text{Vertex}}^2, \quad (17)$$

where χ_{Vertex}^2 is the vertex χ^2 of the kinematic fit to the particles that form the B -meson candidate.

With the above selection criteria, we determine the average signal efficiency over the DP, $\langle \epsilon \rangle_{\text{DP}} = (21.0 \pm 0.2)\%$, with MC simulated data generated using the model described in Ref. [9]. There are 23 683 events in the data sample after the selection shown in Fig. 2.

Approximately 10% of the selected signal events are misreconstructed. Misreconstructed signal events, known as self-cross-feed (SCF), occur when a track or neutral cluster from the other B is assigned to the reconstructed signal candidate. This occurs most often for low-momentum tracks and neutral pions; hence the misreconstructed events are concentrated in the corners of the DP. Since these regions are also where the low-mass resonances overlap significantly with each other, it is important to model the misreconstructed events correctly. We account for misreconstructed events with a resolution function described in Sec. V.

MC events are used to study the background from other B decays (B background). We group the B backgrounds into 19 different classes with similar kinematic and topological properties, collecting those decays where less than 8 events are expected into a single generic class. The B background classes used in this analysis are summarized in

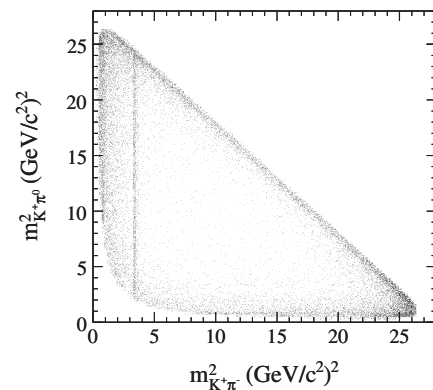


FIG. 2. The DP of the selected data sample of 23 683 events. The selection criteria are described in Sec. IV. The $B^0 \rightarrow \bar{D}^0 \pi^0$ decay is visible as a band near $m_{K^+\pi^-}^2 = 3.5 (\text{GeV}/c^2)^2$. The remaining resonances populate the borders of the DP.

TABLE IV. Summary of B background modes included in the fit model. The expected number of B background events for each mode listed includes the branching fraction and selection efficiency. The D^0X and D^+X classes do not include $B^0 \rightarrow \bar{D}^0\pi^0$ and $B^0 \rightarrow D^-K^+$ decays which are modeled as noninterfering isobars.

Class	B decay	Events	
1	generic	660 ± 122	varied
2	D^0X	627 ± 60	varied
3	D^+X	370 ± 80	varied
4	$K^*(892)^0\gamma, K^*(1430)^0\gamma$	187 ± 14	
5	$K^+\pi^-\pi^+$	164 ± 9	
6	$\pi^+\pi^-\pi^0$	109 ± 13	
7	$K^+\pi^0$	65 ± 3	
8	$K^+\pi^-$	53 ± 2	
9	$\rho^+\rho^0, a_1^0\pi^+, a_1^+\pi^0$	50 ± 13	
10	$f_0(980)K^+, K^{*+}\pi^0$	48 ± 12	
11	$\rho^+\rho^-, a_1^+\pi^-$	27 ± 3	
12	$\eta'K^+$	22 ± 1	
13	$K^{*+}\rho^-$	21 ± 6	
14	$K^{*0}\rho^+$	15 ± 6	
15	$K^{*+}K^-$	14 ± 10	
16	$\rho^+\pi^0$	11 ± 2	
17	$K^{*+}a_1^-, K^{*0}\rho^0$	9 ± 2	
18	$\pi^+\pi^-\pi^+$	8 ± 1	
19	$K^+\eta\pi^-$	8 ± 1	

Table IV. When the yield of a class is varied in the ML fit the quoted number of events corresponds to the fit results, otherwise the expected numbers of selected events are computed by multiplying the MC selection efficiencies by the world average branching fractions [19,23] scaled to the data-set luminosity.

The decay $B^0 \rightarrow K^+\pi^-\pi^0$ is flavor specific (the charge of the kaon identifies the B flavor), so the flavor of the opposite B produced in the decay of the $\Upsilon(4S)$ can be used as additional input in the analysis. Events where the opposite B flavor has been reliably determined are less likely to be either continuum background or SCF. A neural network

is trained using a large sample of MC events with output into seven exclusive tagging categories identifying the flavor of the B meson [24]. Those events where the opposite B flavor could not be determined are included in an untagged category. Each $B^0 \rightarrow K^+\pi^-\pi^0$ decay in the data set is identified with the tagging category of the opposite B determined from the neural network.

V. THE MAXIMUM-LIKELIHOOD FIT

We perform an unbinned extended maximum-likelihood fit to extract the $B^0 \rightarrow K^+\pi^-\pi^0$ event yield and the resonant amplitudes. The fit uses the variables m_{ES} , $\Delta E'$, the NN output, and the DP to discriminate signal from background. The selected on-resonance data sample consists of signal, continuum background, and B background components. The signal likelihood consists of the sum of a correctly reconstructed (truth-matched or TM) and SCF term. The background contributions and fraction of SCF events vary with the tagging category of the opposite B decay. We therefore separate the components of the fit by the tagging category of the opposite B decay.

The likelihood \mathcal{L}_i^c for an event i in tagging category c is the sum of the probability densities of all components,

$$\begin{aligned} \mathcal{L}_i^c \equiv & N_{\text{sig}} f_{\text{sig}}^c [(1 - \langle f_{\text{SCF}} \rangle_{\text{DP}}^c) \mathcal{P}_{\text{TM},i}^c + \langle f_{\text{SCF}} \rangle_{\text{DP}}^c \mathcal{P}_{\text{SCF},i}^c] \\ & + N_{q\bar{q}}^c \frac{1}{2} (1 \pm A_{q\bar{q}}) \mathcal{P}_{q\bar{q},i}^c + \sum_{j=1}^{19} N_{B_j} f_{B_j}^c \frac{1}{2} (1 \pm A_{B_j}) \mathcal{P}_{B_j,i}^c. \end{aligned} \quad (18)$$

Here, j is the B background class number and the (\pm) is evaluated to be the charge sign of the kaon in the event i . A complete summary of the variables in Eq. (18) is given in Table V.

The probability distribution functions (PDFs) \mathcal{P}_X^c ($X = \text{TM}, \text{SCF}, q\bar{q}, B_j$) are the product of the four PDFs of the discriminating variables, $d_1 = m_{ES}$, $d_2 = \Delta E'$, $d_3 = \text{NN}$, and the DP, $d_4 = \{x, y\}$,

TABLE V. Definitions of the different variables in the likelihood function given in Eq. (18).

Variable	Definition
N_{sig}	total number of $K^+\pi^-\pi^0$ signal events in the data sample
f_{sig}^c	fraction of signal events that are tagged in category c
$\langle f_{\text{SCF}} \rangle_{\text{DP}}^c$	fraction of SCF events in tagging category c , averaged over the DP
$\mathcal{P}_{\text{TM},i}^c$	product of PDFs of the discriminating variables used in tagging category c for TM events
$\mathcal{P}_{\text{SCF},i}^c$	product of PDFs of the discriminating variables used in tagging category c for SCF events
$N_{q\bar{q}}^c$	number of continuum events that are tagged in category c
$A_{q\bar{q}}$	parametrizes a possible asymmetry in continuum events
$\mathcal{P}_{q\bar{q},i}^c$	product of PDFs of the discriminating variables used in tagging category c for continuum events
N_{B_j}	number of expected B background events in class j
$f_{B_j}^c$	fraction of B background events that are tagged in category c
A_{B_j}	parametrizes a possible asymmetry in the charged B background in class j
$\mathcal{P}_{B_j,i}^c$	product of PDFs of the discriminating variables used in tagging category c for B background class j

$$\mathcal{P}_{X,i}^c \equiv \prod_{k=1}^4 P_{X,i}^c(d_k). \quad (19)$$

In the fit, the DP coordinates, (x, y) , are transformed to square DP coordinates described in Ref. [9]. The extended likelihood over all tagging categories is given by

$$\mathcal{L} \equiv \prod_{c=1}^7 e^{-N^c} \prod_i^{N^c} \mathcal{L}_i^c, \quad (20)$$

where N^c is the total number of events in tagging category c . The parametrizations of the PDFs are described in Sec. VA and Sec. VB.

A. The Dalitz plot PDFs

Since the decay $B^0 \rightarrow K^+ \pi^- \pi^0$ is flavor specific, the B^0 and \bar{B}^0 DP distributions are independent of each other and in general can differ due to CP violating effects. The backgrounds, however, are largely independent of the B flavor, hence a more reliable estimate of their contribution is obtained by fitting the B^0 and \bar{B}^0 DP distributions simultaneously. We describe only the B^0 DP PDF, since a change from \mathcal{A} to $\bar{\mathcal{A}}$ accompanied by the interchange of

the charges of the kaon and pion gives the \bar{B}^0 PDF. Projections of the DP are shown for each of the invariant masses $m_{\pi^- \pi^0}$ in Fig. 3, $m_{K^+ \pi^0}$ in Fig. 4, and $m_{K^+ \pi^-}$ in Fig. 5 along with the data.

1. Signal

The total $B^0 \rightarrow K^+ \pi^- \pi^0$ amplitude is given by

$$\mathcal{A}(x, y) = \sum_k a_k e^{i\Phi_k} f_k(J, x, y), \quad (21)$$

where k runs over all of components in the model described in Sec. II. The amplitudes and phases are measured relative to the $\rho(770)^- K^+$ amplitude so that the phases $\Phi_{\rho(770)^- K^+}$ and $\bar{\Phi}_{\rho(770)^+ K^-}$ are fixed to 0 and the isobar, $\bar{a}_{\rho(770)^- K^+}$, is fixed to 1. The TM signal DP PDF is

$$P_{\text{TM}}(x, y) = \epsilon(x, y)(1 - f_{\text{SCF}}(x, y)) \frac{|\mathcal{A}|^2}{|N_{\text{TM}}|^2}, \quad (22)$$

where

$$|N_{\text{TM}}|^2 = \text{Re} \sum_{\kappa, \sigma} a_{\kappa} a_{\sigma} e^{i(\Phi_{\kappa} - \Phi_{\sigma})} \langle \text{TM} | f_{\kappa} f_{\sigma}^* \rangle_{\text{DP}}, \quad (23)$$

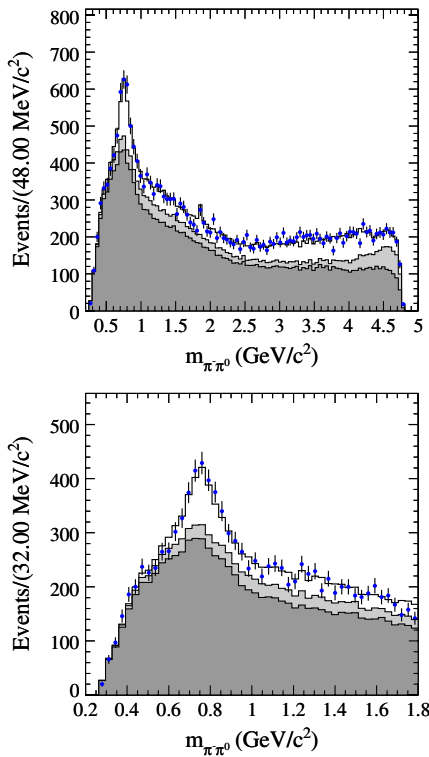


FIG. 3 (color online). The $m_{\pi^- \pi^0}$ invariant mass distributions in the entire kinematic range (top) and below $1.8 \text{ GeV}/c^2$ (bottom) for all selected events. The $\rho(770)^-$ is visible as a broad peak near $0.77 \text{ GeV}/c^2$. The data are shown as points with error bars. The solid histograms show the projection of the fit result for charmless signal and D events (white), B background (medium), and continuum (dark).

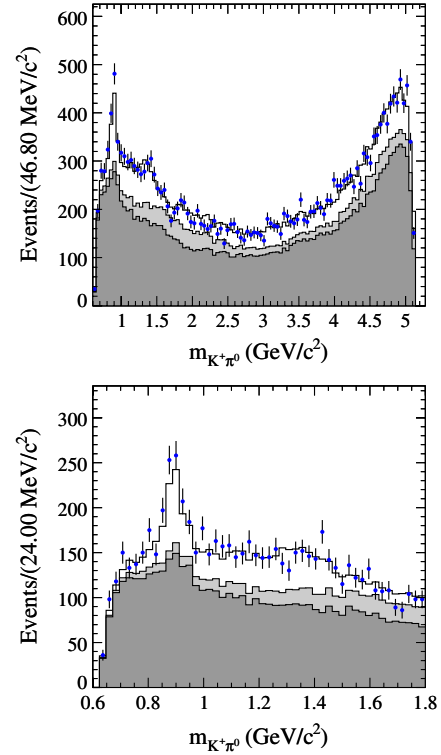


FIG. 4 (color online). The $m_{K^+ \pi^0}$ invariant mass distributions in the entire kinematic range (top) and below $1.8 \text{ GeV}/c^2$ (bottom) for all selected events. The $K^*(892)^+$ is visible as a narrow peak near $0.89 \text{ GeV}/c^2$ while the broad distribution near $1.40 \text{ GeV}/c^2$ is the $(K\pi)_0^{*+}$. The data are shown as points with error bars. The solid histograms show the projection of the fit result for charmless signal and D events (white), B background (medium), and continuum (dark).

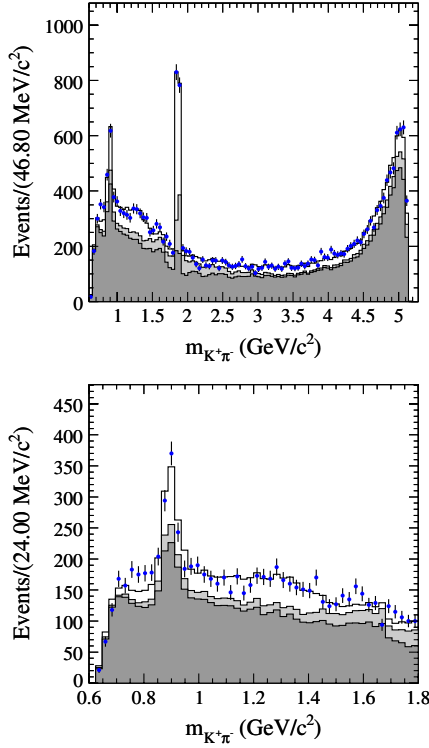


FIG. 5 (color online). The $m_{K^+\pi^-}$ invariant mass distributions in the entire kinematic range (top) and below $1.8 \text{ GeV}/c^2$ (bottom) for all selected events. The $K^*(892)^0$ is visible as a narrow peak near $0.89 \text{ GeV}/c^2$ while the broad distribution near $1.40 \text{ GeV}/c^2$ is the $(K\pi)_0^{*0}$. The narrow peak near $1.8 \text{ GeV}/c^2$ is the D^0 meson. The data are shown as points with error bars. The solid histograms show the projection of the fit result for charmless signal and D events (white), B background (medium), and continuum (dark).

and

$$\langle \text{TM} | f_\kappa f_\sigma^* \rangle_{\text{DP}} = \int_{\text{DP}} \epsilon(x, y) (1 - f_{\text{SCF}}(x, y)) f_\kappa f_\sigma^* dx dy. \quad (24)$$

Here, $\epsilon(x, y)$ and $f_{\text{SCF}}(x, y)$ are the DP-dependent signal selection efficiency and SCF fraction. These are implemented as histograms in the square DP coordinates. The indices κ, σ run over all components of the signal model. Equation (24) is evaluated numerically for the line shapes described in Sec. II.

The PDF for signal SCF is given by

$$P_{\text{SCF}}(x, y) = \epsilon(x, y) f_{\text{SCF}}(x, y) \frac{|\mathcal{A}|^2 \otimes R_{\text{SCF}}}{|N_{\text{SCF}}|^2 \otimes R_{\text{SCF}}}, \quad (25)$$

where $|N_{\text{SCF}}|^2$ is given by Eq. (23) with the replacement $\text{TM} \rightarrow \text{SCF}$, and

$$\langle \text{SCF} | f_\kappa f_\sigma^* \rangle_{\text{DP}} = \int_{\text{DP}} \epsilon(x, y) f_{\text{SCF}}(x, y) f_\kappa f_\sigma^* dx dy. \quad (26)$$

Convolution with a resolution function is denoted by $\otimes R_{\text{SCF}}$. In contrast with TM events, a convolution is

necessary for SCF, since misreconstructed events often incur large migrations over the DP, *i.e.* the reconstructed coordinates (x_r, y_r) are far from the true values (x_t, y_t) . MC data sets are used to study this effect and we find that misreconstructed resonances can be broadened by as much as 800 MeV . We introduce a resolution function, $R_{\text{SCF}}(x_r, y_r; x_t, y_t)$, which represents the probability to reconstruct at the coordinates (x_r, y_r) a SCF event that has the true coordinate (x_t, y_t) . The resolution function is normalized so that

$$\int_{\text{DP}} R_{\text{SCF}}(x_r, y_r; x_t, y_t) dx_r dy_r = 1 \forall (x_t, y_t), \quad (27)$$

and is implemented as an array of two-dimensional histograms that store the probabilities as a function of the DP coordinates. R_{SCF} is convolved with the signal model in the expression of \mathcal{P}_{SCF} in Eq. (25) to correct for broadening of the SCF events.

The normalization of the total signal PDF is guaranteed by the DP averaged fraction of SCF events,

$$\langle f_{\text{SCF}} \rangle_{\text{DP}}^c = \frac{\int_{\text{DP}} \epsilon(x, y) f_{\text{SCF}}^c(x, y) (|\mathcal{A}|^2 + |\bar{\mathcal{A}}|^2) dx dy}{\int_{\text{DP}} \epsilon(x, y) (|\mathcal{A}|^2 + |\bar{\mathcal{A}}|^2) dx dy}. \quad (28)$$

This quantity is decay dynamics-dependent, and in principle must be computed iteratively. Typically, $\langle f_{\text{SCF}} \rangle_{\text{DP}}^c \approx 9\%$ converging rapidly after a small number of fits.

2. Background

The continuum DP distribution is extracted from a combination of off-resonance data and an m_{ES} sideband ($5.200 \text{ GeV}/c^2 \leq m_{\text{ES}} \leq 5.272 \text{ GeV}/c^2$) of the on-resonance data from which the B background has been subtracted. The DP is divided into eight regions where different smoothing parameters are applied in order to optimally reproduce the observed wide and narrow structures by using a two-dimensional kernel estimation technique [25]. A finely binned histogram is used to describe the peak from the narrow D^0 continuum production. Most B background DP PDFs are smoothed two-dimensional histograms obtained from MC. The backgrounds due to $b \rightarrow c$ decays with D^0 mesons (class 2 in Table IV) are modeled with a finely binned histogram around the D^0 mass.

B. Description of the other variables

1. Signal

The m_{ES} distribution for TM-signal events is parameterized by a modified Gaussian distribution given by

$$P_{\text{sig-TM}}(d_1) = \exp\left[-\frac{(d_1 - m)^2}{2\sigma_\pm^2 + \alpha_\pm(d_1 - m)^2}\right]. \quad (29)$$

The peak of the distribution is given by m and the asymmetric width of the distribution σ_\pm is given by σ_+ for $d_1 < m$ and σ_- for $m < d_1$. The asymmetric modulation α_\pm is similarly given by α_+ for $d_1 < m$ and α_- for

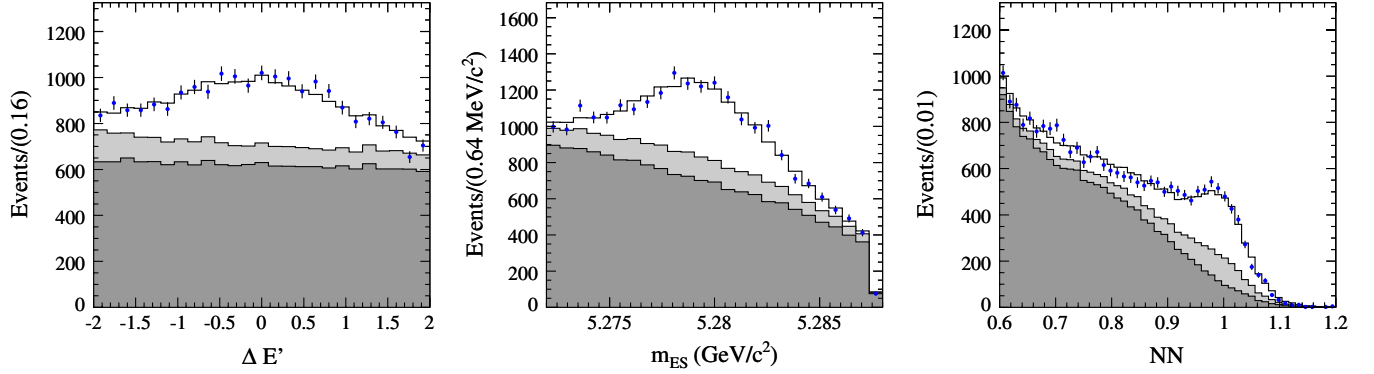


FIG. 6 (color online). Distributions of $\Delta E'$ (left), m_{ES} (center), and NN output (right) for all selected events. The data are shown as points with error bars. The solid histograms show the projection of the fit result for charmless signal and D events (white), B background (medium) and continuum (dark).

$m < d_1$. The parameters in Eq. (29) are determined in the data fit. The m_{ES} distribution for SCF-signal events is a smoothed histogram produced with a Gaussian kernel estimation technique from MC.

The $\Delta E'$ distribution for TM-signal events is parametrized by the sum of a Gaussian and a first-order polynomial PDF,

$$P_{\text{sig-TM}}(d_2) = \frac{1}{\sigma} \exp\left[-\frac{(d_2 - m)^2}{2\sigma^2}\right] + ad_2 + b. \quad (30)$$

The parameters m , σ , a given in Eq. (30) are described by linear functions of $x = m_{K^\pm\pi^\mp}^2$ with slopes and intercepts determined in the fit in order to account for a small residual correlation of $\Delta E'$ with the DP position. A smoothed histogram taken from MC is used for the SCF-signal $\Delta E'$ PDF. The NN PDFs for signal events are smoothed histograms taken from MC.

2. Background

We use the ARGUS function [26]

$$P_{q\bar{q}}\left(z = \frac{d_1}{m_{ES}^{\max}}\right) \propto z\sqrt{1-z^2}e^{-\xi(1-z^2)}, \quad (31)$$

as the continuum m_{ES} PDF. The end point m_{ES}^{\max} is fixed to 5.2897 GeV/ c^2 and ξ is determined in the fit. The continuum $\Delta E'$ PDF is a linear function with slope determined in the fit. The shape of the continuum NN distribution is correlated with the DP position and is described by a function that varies with the closest distance between the point representing the event and the boundary of the DP Δ_{DP} ,

$$P_{q\bar{q}}(d_3; \Delta_{DP}) = (1 - d_3)^{k_1}(k_2 d_3^2 + k_3 d_3 + k_4). \quad (32)$$

Here, $k_i = q_i + p_i \cdot \Delta_{DP}$, where q_i , p_i are determined in the fit. We use smoothed histograms taken from MC to describe m_{ES} , $\Delta E'$, and NN distributions for the B background classes in Table IV. Projections of the m_{ES} , $\Delta E'$,

and NN PDFs are shown in Fig. 6 for signal, B background, and continuum events along with the data.

VI. RESULTS

The ML fit results in a charmless signal yield of $N_{\text{sig}} = 3670 \pm 96(\text{stat}) \pm 94(\text{syst})$ events and total branching fraction for charmless $B^0 \rightarrow K^+ \pi^- \pi^0$ decays of $\mathcal{B}_{\text{sig}} = 38.5 \pm 1.0(\text{stat}) \pm 3.9(\text{syst}) \times 10^{-6}$. We find the yields for $B^0 \rightarrow \bar{D}^0 \pi^0$ and $B^0 \rightarrow D^- K^+$ events are consistent with the expectations based on their world average branching fractions. The sources of systematic uncertainty, including those related to the composition of the DP, are discussed in Sec. VII. When the fit is repeated starting from input parameter values randomly distributed within the statistical uncertainty of the values obtained from the ML fit for the magnitudes, and within the $[-\pi, \pi]$ interval for the phases, we observe convergence toward four minima of the negative log-likelihood function ($\text{NLL} = -\log \mathcal{L}$). The best solution is separated by 5.4 units of NLL (3.3σ) from the next best solution. The event yield we quote is for the best solution; the spread of signal yields between the four solutions is less than five events. The phases Φ and $\bar{\Phi}$, CP asymmetries and branching fractions determined by the ML fit are given for the best solution in Table VI. We quote the total branching fractions in Table VI assuming all $K^* \rightarrow K\pi$ and $\rho \rightarrow \pi^+\pi^-$ branching fractions to be 100% and isospin conservation in $K^* \rightarrow K\pi$ decays. In the Appendix we list the fitted magnitudes and phases for the four solutions together with the correlation matrix for the best solution.

We measure the relative phase between the narrow $B^0 \rightarrow K^*(892)^+ \pi^-$ and $B^0 \rightarrow K^*(892)^0 \pi^0$ resonances despite their lack of kinematic overlap due to significant contributions from the $B^0 \rightarrow (K\pi)_0^* \pi^0$, $(K\pi)_0^* \pi^-$ S-waves, $B^0 \rightarrow \rho(770)^- K^+$, and NR components. Each of these components interferes with both the $B^0 \rightarrow K^*(892)^+ \pi^-$ and $B^0 \rightarrow K^*(892)^0 \pi^0$ resonances, providing a mechanism for their coherence. The relative phases among the resonances

TABLE VI. CP averaged branching fractions \mathcal{B}_k , phases $\bar{\Phi}$ and Φ for \bar{B}^0 and B^0 decays, respectively, measured relative to $B^0(\bar{B}^0) \rightarrow \rho(770)^\mp K^\pm$, and CP asymmetries, A_{CP} , defined in Eq. (7). The first error is statistical and the second is systematic. When the elastic range term is separated from the $K\pi$ S-wave we determine the total NR branching fraction $\mathcal{B}_{\text{NR}} = 7.6 \pm 0.5(\text{stat}) \pm 1.0(\text{syst}) \times 10^{-6}$ and the resonant $K_0^*(1430)\pi$ branching fractions $\mathcal{B}_{K_0^*(1430)^+\pi^-} = 27.8 \pm 2.5(\text{stat}) \pm 3.3(\text{syst}) \times 10^{-6}$, $\mathcal{B}_{K_0^*(1430)^0\pi^0} = 7.0 \pm 0.5(\text{stat}) \pm 1.1(\text{syst}) \times 10^{-6}$.

Isobar	$\mathcal{B} (\times 10^{-6})$	$\bar{\Phi} [^\circ]$	$\Phi [^\circ]$	A_{CP}
$\rho(770)^- K^+$	$6.6 \pm 0.5 \pm 0.8$	0 (fixed)	0 (fixed)	$0.20 \pm 0.09 \pm 0.08$
$\rho(1450)^- K^+$	$2.4 \pm 1.0 \pm 0.6$	$75 \pm 19 \pm 9$	$126 \pm 25 \pm 26$	$-0.10 \pm 0.32 \pm 0.09$
$\rho(1700)^- K^+$	$0.6 \pm 0.6 \pm 0.4$	$18 \pm 36 \pm 16$	$50 \pm 38 \pm 20$	$-0.36 \pm 0.57 \pm 0.23$
$K^{*}(892)^+ \pi^-$	$8.0 \pm 1.1 \pm 0.8$	$33 \pm 22 \pm 20$	$39 \pm 25 \pm 20$	$-0.29 \pm 0.11 \pm 0.02$
$K^{*}(892)^0 \pi^0$	$3.3 \pm 0.5 \pm 0.4$	$29 \pm 18 \pm 6$	$17 \pm 20 \pm 8$	$-0.15 \pm 0.12 \pm 0.04$
$(K\pi)_0^{*+} \pi^-$	$34.2 \pm 2.4 \pm 4.1$	$-167 \pm 16 \pm 37$	$-130 \pm 22 \pm 22$	$0.07 \pm 0.14 \pm 0.01$
$(K\pi)_0^{*0} \pi^0$	$8.6 \pm 1.1 \pm 1.3$	$13 \pm 17 \pm 12$	$10 \pm 17 \pm 16$	$-0.15 \pm 0.10 \pm 0.04$
NR	$2.8 \pm 0.5 \pm 0.4$	$48 \pm 14 \pm 6$	$90 \pm 21 \pm 15$	$0.10 \pm 0.16 \pm 0.08$

are consequently sensitive to the models for their kinematic shapes. We discuss the systematic uncertainty associated with mismodeling of the resonance shapes in Sec. VII.

The quality of the fit to the DP is appraised from a χ^2 of 745 for 628 bins where at least 16 events exist in each bin. The relatively poor fit appears to be due to mismodeling of the continuum background which comprises 69% of the 23 683 events. A signal enhanced subsample of 3232

events is selected by requiring the signal likelihood of events to be greater than 20% as determined by the product of the NN, $\Delta E'$, and m_{ES} PDFs. Using the signal enhanced subsample we find a χ^2 of 149 for 140 bins where at least 16 events exist in each bin. The excess events near $0.8 \text{ GeV}/c^2$ seen in Fig. 5 are not observed in the signal enhanced subsample. The systematic uncertainty associated with continuum mismodeling is described in Sec. VII.

We validate the fit model by generating 100 data sample sized pseudoexperiments with the same isobar values as the best solution, and observe that the NLL of the data fit falls within the NLL distribution of the pseudoexperiments. The distributions of log-likelihood ratio, $\log(\mathcal{L}_{\text{sig}}/\mathcal{L})$ [see Eq. (18)], are shown in Fig. 7. The distributions show good agreement of the data with the fit model. The agreement remains good when events near the D^0 region of the DP ($1.8 \text{ GeV}/c^2 < m_{K^+\pi^-} < 1.9 \text{ GeV}/c^2$) are removed from the log-likelihood distribution.

VII. SYSTEMATIC UNCERTAINTIES

Since the amount of time required for the likelihood fit to converge dramatically increases with the number of isobar parameters to determine, we limit our isobar model to only those resonances with significant branching fractions. The dominant systematic uncertainty in this analysis is due to contributions from intermediate resonances not included in the isobar model. We include the $K^*(1680)\pi$ and tensor $K_2^*(1430)\pi$ resonances with line shapes described in Table VII in a fit to data. The result of this fit is used to generate high statistics samples of MC including these resonances. These samples are then fitted with the nominal isobar model and the observed shifts in the isobar parameters are listed as the Isobar model systematic uncertainty in the Appendix. We find the $K^*(1680)\pi$ and $K_2^*(1430)\pi$ amplitudes each to contribute less than 1% of the charmless signal yield.

Mismodeling of the continuum DP (CDP) distribution is the second most significant source of systematic uncertainty in the isobar parameters of the signal DP model.

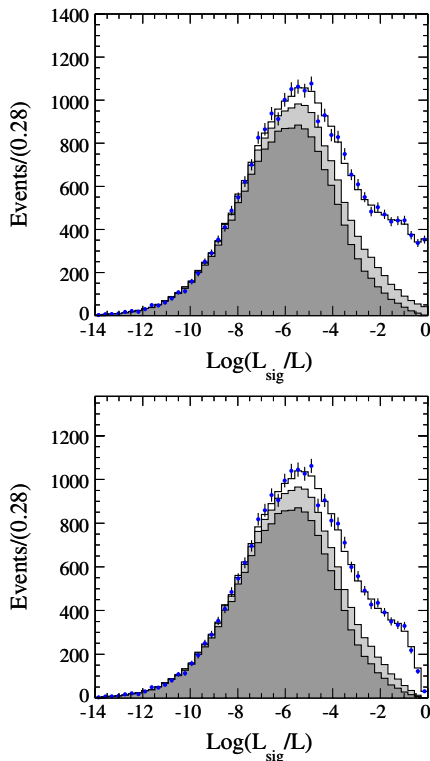


FIG. 7 (color online). Distributions of the log-likelihood for all events (top) and for events excluding the D^0 region $1.8 \text{ GeV}/c^2 < m_{K^+\pi^-} < 1.9 \text{ GeV}/c^2$ (bottom). The data are shown as points with error bars. The solid histograms show the projection of the fit result for charmless signal and D events (white), B background (medium), and continuum (dark).

TABLE VII. The line shape parameters of the additional $K_2^*(1430)^0$, $K_2^*(1430)^+$, $K^*(1680)^0$ and $K^*(1680)^+$ resonances.

Resonance	Line shape	Parameters
	Spin- $J = 1$	
$K^*(1680)^0$	RBW [19]	$M = 1717 \text{ MeV}/c^2$ $\Gamma^0 = 322 \text{ MeV}$ $R = 1.5 \text{ (GeV)}^{-1}$
$K^*(1680)^+$	RBW [19]	$M = 1717 \text{ MeV}/c^2$ $\Gamma^0 = 322 \text{ MeV}$ $R = 1.5 \text{ (GeV)}^{-1}$
	Spin $J = 2$	
$K_2^*(1430)^0$	RBW [19]	$M = 1432 \text{ MeV}/c^2$ $\Gamma^0 = 109 \text{ MeV}$ $R = 1.5 \text{ (GeV)}^{-1}$
$K_2^*(1430)^+$	RBW [19]	$M = 1425 \text{ MeV}/c^2$ $\Gamma^0 = 98.5 \text{ MeV}$ $R = 1.5 \text{ (GeV)}^{-1}$

Because of the limited amount of off-resonance events recorded at *BABAR*, the CDP distribution is modeled from the m_{ES} sideband as described in Sec. IV. Events in the m_{ES} sideband have necessarily higher momentum than those near the signal peak and hence have a different DP distribution. To quantify the effect of modeling the m_{ES} on-resonance CDP with off-resonance events we use a high statistics sample of $q\bar{q}$ MC to create a model of the CDP from the m_{ES} signal region. We then generate 100 pseudoexperiments with the m_{ES} signal region CDP model and fit each of these with both the on-resonance and off-resonance models of the CDP. The average difference observed in the isobar parameters between fits with each of the CDP models is recorded as the Continuum DP systematic uncertainty in the Appendix. In order to quantify the effect of mismodeling of the shape of the continuum DP with the nominal smoothing parameter, we recreate the continuum DP PDF with various smoothing parameters. We refit the data using these alternate continuum DP PDFs and record the variations in the isobars as the PDF shape systematic uncertainty in the Appendix.

Other sources of systematic uncertainty include: the uncertainty in the masses and widths of the resonances, the uncertainty in the fixed B background yields, the intrinsic bias in the fitting procedure, and the misestimation of SCF and particle identification (PID) efficiencies in MC. We vary the masses, widths, and other resonance parameters within the uncertainties quoted in Table II, and assign the observed differences in the measured amplitudes as systematic uncertainties (Line shape systematic uncertainty in the Appendix). We find that variations of the radius R do not significantly change the fitted values of the isobar parameters. To estimate the systematic uncertainty due to fixing the B background yields, we float each of the B background contributions in a series of fits to data. We record the variation in the isobar parameters as the B background systematic uncertainty in the Appendix.

The intrinsic fit bias is estimated from the average deviation in the fitted isobar parameters from their generated values in an ensemble of fits to MC data sets generated with the expected yields of signal, continuum and B background events. The average deviation in the isobar parameters from their generated values in MC data sets is recorded as the Fit bias systematic uncertainty in the Appendix.

The average fraction of misreconstructed signal events predicted by MC has been verified with fully reconstructed $B \rightarrow D\rho$ events [27]. No significant differences between data and the simulation are found. We estimate the effect of misestimating the SCF fractions in MC by varying their nominal values relatively by $\pm 10\%$ in a pair of fits to data. The average shift in the isobar parameters is recorded as the SCF fraction systematic uncertainty in the Appendix.

The efficiency to identify a particle correctly in the detector differs slightly for MC and data. Since the efficiency across the DP is measured using MC samples, we must apply a PID weighting to each reconstructed event in order to produce a corrected DP efficiency. We refit the data set with the PID corrected DP and record the shift in the isobar parameters as the PID systematic uncertainty in the Appendix.

VIII. INTERPRETATION

Here, we use the results of this analysis and that presented for $B^0 \rightarrow K_S^0 \pi^+ \pi^-$ [5] to construct isospin amplitudes as described by Eqs. (1) and (2). Individually, the phases of these amplitudes provide sensitivity to the CKM angle γ while together they have been shown to obey the sum rule defined in Eq. (3) in the limit of SU(3) symmetry.

A. Measurement of $\Phi_{3/2}$

1. $B \rightarrow K^* \pi$ decays

The weak phase of $\mathcal{A}_{3/2}$ in Eq. (1), expressed as a function of the phases and magnitudes of isobar amplitudes, is given by [6]

$$\Phi_{3/2} = \frac{1}{2}(\delta - \bar{\delta} + \Delta\phi_{K^*\pi}). \quad (33)$$

Here,

$$\delta = \arctan\left(\frac{\sqrt{2}|\mathcal{A}_{K^*0\pi^0}^{(-)} s^{(-)}}{|\mathcal{A}_{K^*+\pi^-}^{(-)}| + \sqrt{2}|\mathcal{A}_{K^*0\pi^0}^{(-)}| c^{(-)}}\right), \quad (34)$$

and $\mathcal{A}_{K^*0\pi^0}^{(-)}$, $\mathcal{A}_{K^*+\pi^-}^{(-)}$ are the isobar amplitudes given in Eq. (4). We define

$$s^{(-)} = \sin(\Phi_{K^*0\pi^0}^{(-)} - \Phi_{K^*+\pi^-}^{(-)}), \quad (35)$$

$$c^{(-)} = \cos(\Phi_{K^*0\pi^0}^{(-)} - \Phi_{K^*+\pi^-}^{(-)}), \quad (36)$$

$$\Delta\phi_{K^*\pi} = \Phi_{K^*+\pi^-} - \bar{\Phi}_{K^*-\pi^+}. \quad (37)$$

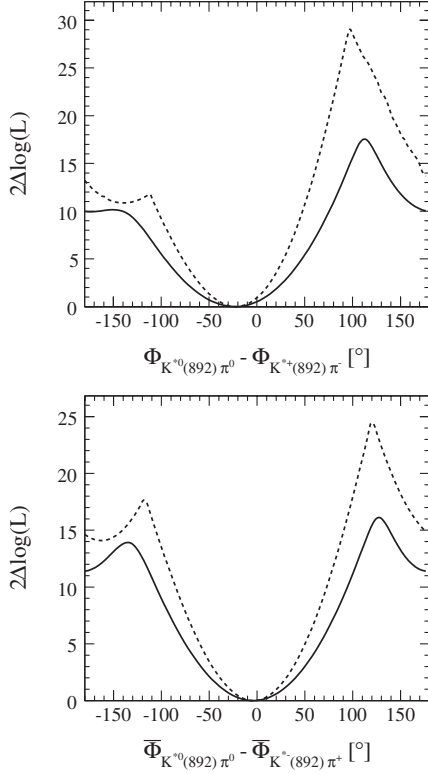


FIG. 8. Likelihood scans illustrating the measurements of $\Phi_{K^{*0}\pi^0} - \Phi_{K^{*+}\pi^-} = -22 \pm 24(\text{stat}) \pm 18(\text{syst})^\circ$ (top) and $\Phi_{K^{*0}\pi^0} - \Phi_{K^{*-}\pi^+} = -4 \pm 24(\text{stat}) \pm 19(\text{syst})^\circ$ (bottom). The solid (dashed) line shows the $2\Delta \log(L)$ for the total (statistical) uncertainty.

Likelihood scans illustrating the measurements of $\Phi_{K^{*0}\pi^0} - \Phi_{K^{*+}\pi^-}$ are shown in Fig. 8. We measure $\Phi_{K^{*0}\pi^0} - \Phi_{K^{*+}\pi^-} = -22 \pm 24(\text{stat}) \pm 18(\text{syst})^\circ$ and $\Phi_{K^{*0}\pi^0} - \Phi_{K^{*-}\pi^+} = -4 \pm 24(\text{stat}) \pm 19(\text{syst})^\circ$ using the helicity convention defined in Fig. 1. We use $\Delta\phi_{K^*\pi} = 58 \pm 33(\text{stat}) \pm 9(\text{syst})^\circ$ [5] and subtract the mixing phase contribution $2\beta = 42.2 \pm 1.8^\circ$ [23] to evaluate Eq. (33).

It is important to note that for vector resonances the helicity convention defines an ordering of particles in the final state via the angular dependence $T(J, x, y)$ (Table I). This means that care must be taken to use a consistent helicity convention when evaluating an isospin decomposition of vector amplitudes [28]. In this analysis the helicity angle for $K^{*+}\pi^-$ is measured between the K^+ and π^- while the helicity angle for $K^{*0}\pi^0$ is measured between the

π^- and π^0 . This results in a sign flip between the $\mathcal{A}_{K^{*0}\pi^0}^{(-)}$, $\mathcal{A}_{K^{*+}\pi^-}^{(-)}$ amplitudes when Eq. (1) is evaluated with $K^*(892)\pi$ amplitudes measured as in Table VI. The $\mathcal{A}_{3/2}(K^*\pi)$ isospin triangles described by Eq. (1) are shown in Fig. 9 for the $K^*(892)\pi$ amplitudes measured in Table VI. The destructive interference between

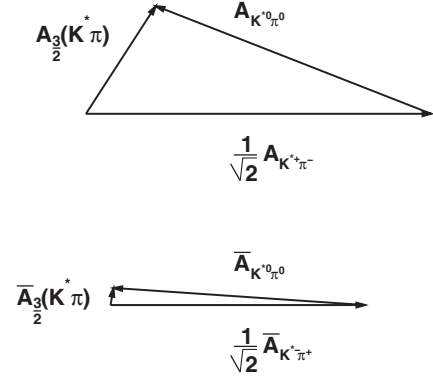


FIG. 9. Isospin triangles drawn to scale for $B \rightarrow K^*\pi$ decays. The isobar amplitudes are summarized in Table VIII as solution I. Note that the isospin triangle for \bar{B} decays is relatively flat and $\bar{\mathcal{A}}_{3/2}(K^*\pi)$ is consistent with 0.

$K^*(892)\pi$ amplitudes in the isospin decomposition (Fig. 9) is expected, since these amplitudes are penguin-dominated while $\mathcal{A}_{3/2}^{(-)}$ is penguin-free by construction [28]. We find that $\mathcal{A}_{3/2}(K^*\pi)$ is consistent with 0 and consequently that the uncertainty in $\bar{\delta}$ is too large to permit a measurement of $\Phi_{3/2}$ using $K^*(892)\pi$ amplitudes as originally suggested in Ref. [3].

2. $B \rightarrow \rho K$ decays

It is also possible to obtain a CKM constraint using $B \rightarrow \rho K$ decay amplitudes as in Eq. (2). Here, the $\rho^- K^+$ and $\rho^0 K^0$ amplitudes do not decay to a common final state, making a direct measurement of their relative phase impossible. Interference between $\rho^- K^+$ and $\rho^0 K^0$ amplitudes and $K^{*+}\pi^-$ can be observed using B^0 decays to both $K^+\pi^-\pi^0$ and $K_S^0\pi^+\pi^-$, permitting an indirect measurement of their relative phase. The weak phase of $\mathcal{A}_{3/2}(\rho K)$ is given by Eq. (33), where now

$$\bar{\delta} = \arctan\left(\frac{|\mathcal{A}_{\rho^-K^+}|_{S^-}^{(-)} + \sqrt{2}|\mathcal{A}_{\rho^0K^0}|_{S^0}^{(-)}}{|\mathcal{A}_{\rho^-K^+}|_{C^-}^{(-)} + \sqrt{2}|\mathcal{A}_{\rho^0K^0}|_{C^0}^{(-)}}\right). \quad (38)$$

Here we define

$$|_{S^-}^{(-)} = \sin(\Phi_{\rho^-K^+}^{(-)} - \Phi_{K^{*+}\pi^-}^{(-)}), \quad (39)$$

$$|_{C^-}^{(-)} = \cos(\Phi_{\rho^-K^+}^{(-)} - \Phi_{K^{*+}\pi^-}^{(-)}), \quad (40)$$

$$|_{S^0}^{(-)} = \sin(\Phi_{\rho^0K^0}^{(-)} - \Phi_{K^{*+}\pi^-}^{(-)}), \quad (41)$$

$$|_{C^0}^{(-)} = \cos(\Phi_{\rho^0K^0}^{(-)} - \Phi_{K^{*+}\pi^-}^{(-)}). \quad (42)$$

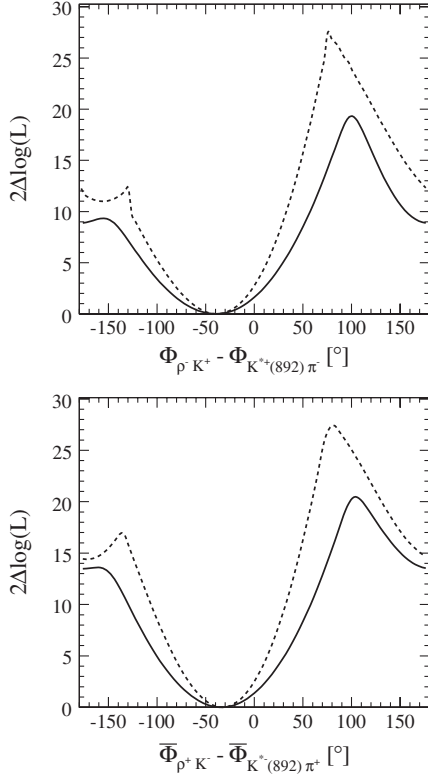


FIG. 10. Likelihood scans illustrating the measurements of $\Phi_{\rho^-K^+} - \Phi_{K^{*+}\pi^-} = -33 \pm 22(\text{stat}) \pm 20(\text{syst})^\circ$ (top) and $\Phi_{\rho^+K^-} - \Phi_{K^{*-}\pi^+} = -39 \pm 25(\text{stat}) \pm 20(\text{syst})^\circ$ (bottom). The solid (dashed) line shows the $2\Delta \log(L)$ for the total (statistical) uncertainty.

We use the $K^{*}(892)^+\pi^-$ amplitude in the evaluation of these expressions. Likelihood scans of the phase differences $\Phi_{\rho^-K^+} - \Phi_{K^{*+}\pi^-}$ are shown in Fig. 10. We measure $\Phi_{\rho^-K^+} - \Phi_{K^{*+}\pi^-} = -33 \pm 22(\text{stat}) \pm 20(\text{syst})^\circ$ and $\Phi_{\rho^+K^-} - \Phi_{K^{*-}\pi^+} = -39 \pm 25(\text{stat}) \pm 20(\text{syst})^\circ$.

We use the measurements $\Phi_{\rho^0K^0} - \Phi_{K^{*+}\pi^-} = 174 \pm 28(\text{stat}) \pm 15(\text{syst})^\circ$ and $\Phi_{\rho^0K^0} - \Phi_{K^{*-}\pi^+} = -148 \pm 25(\text{stat}) \pm 16(\text{syst})^\circ$ given in Ref. [5]. Before evaluating Eq. (38) we must account for any discrepancy in helicity conventions used in this analysis and Ref. [5]. Here we must consider the helicity conventions used not only by the ρK amplitudes but also the intermediate $K^{*}(892)^+\pi^-$ amplitude. In this analysis the helicity angle is measured between the π^0 and K^+ for ρ^-K^+ amplitudes while the helicity angle is measured between the π^- and K^0 in Ref. [5]. It is also the case that the helicity angle is measured between the π^+ and π^- for K^{*+} decays in Ref. [5], and is measured between the K^+ and π^- in this analysis. Since there are a total of two sign flips due to these differences there is no net sign flip between $\mathcal{A}_{\rho^0K^0}$ and $\mathcal{A}_{\rho^-K^+}$ when Eq. (2) is evaluated using the measurements presented in this article and in Ref. [5].

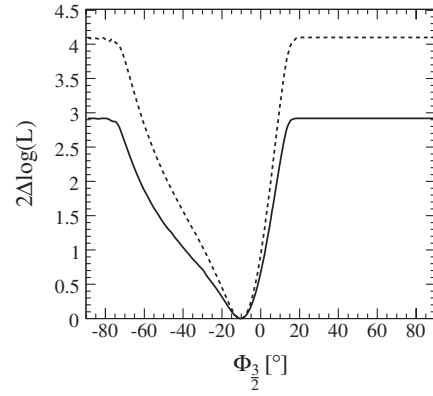


FIG. 11. Likelihood scans illustrating the measurement of $\Phi_{3/2} = -10^{+10}(\text{stat})^{+7}(\text{syst})^\circ$. The solid (dashed) line shows the $2\Delta \log(L)$ for the total (statistical) uncertainty.

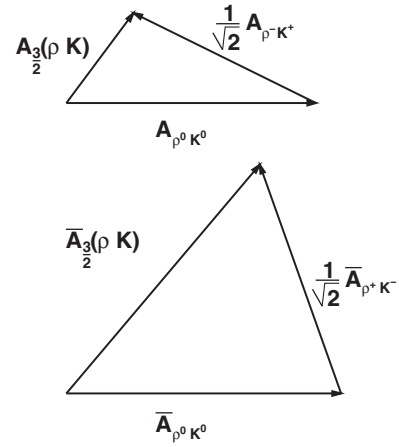


FIG. 12. Isospin triangles drawn to scale for $B \rightarrow \rho K$ decays. The isobar amplitudes are summarized in Table VIII as solution I and in Ref. [5].

We evaluate Eq. (33) using Eq. (38) and produce a measurement of $\Phi_{3/2}$ illustrated in Fig. 11. The $\mathcal{A}_{3/2}(\rho K)$ isospin triangles described by Eq. (2) are shown in Fig. 12 for the $B \rightarrow \rho K$ amplitudes measured in this analysis and Ref. [5]. In contrast to the $K^*\pi$ isospin triangles (Fig. 9) both $\mathcal{A}_{3/2}(\rho K)$ are significantly different from 0 permitting a measurement of $\Phi_{3/2} = -10^{+10}(\text{stat})^{+7}(\text{syst})^\circ$. This measurement is defined modulo 180° [see Eq. (33)] and we quote only the value between $\pm 90^\circ$. The likelihood constraint shown in Fig. 11 becomes flat, since sufficiently large deviations of the $B \rightarrow \rho K$ amplitudes will result in a flat isospin triangle and consequently an arbitrary value of $\Phi_{3/2}$.

B. Evaluation of the amplitude sum rule

The sum rule given in Eq. (3) motivates the definition of the dimensionless quantity

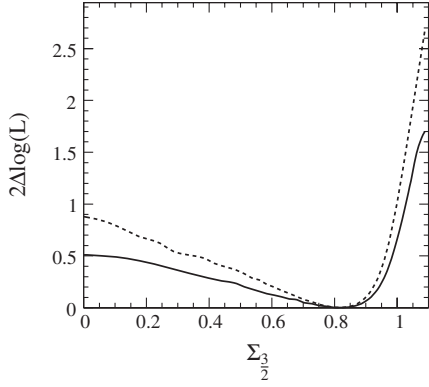


FIG. 13. Likelihood scan for $\Sigma_{3/2}$. The solid (dashed) line shows the $2\Delta \log(L)$ for the total (statistical) uncertainty. We measure $\Sigma_{3/2} = 0.82_{-0.92}^{+0.18}(\text{stat})_{-1.35}^{+0.11}(\text{syst})$.

$$\Sigma_{3/2} = \frac{|\bar{\mathcal{A}}_{3/2}(K^*\pi)|^2 - |\mathcal{A}_{3/2}(K^*\pi)|^2}{|\bar{\mathcal{A}}_{3/2}(\rho K)|^2 - |\mathcal{A}_{3/2}(\rho K)|^2} + 1. \quad (43)$$

The asymmetry parameter $\Sigma_{3/2}$ will be 0 in the limit of exact SU(3) symmetry. Deviations from exact SU(3) symmetry or contributions from new physics operators can be quantified, if $\Sigma_{3/2}$ is measured to be significantly different from 0. We use the amplitudes and phase differences among $B^0 \rightarrow K^*\pi$ and $B^0 \rightarrow \rho K$ amplitudes as described in Sec. VIII A to produce a likelihood scan of $\Sigma_{3/2}$ as shown in Fig. 13. We measure $\Sigma_{3/2} = 0.82_{-0.92}^{+0.18}(\text{stat})_{-1.35}^{+0.11}(\text{syst})$, consistent with 0. The large statistical and systematic uncertainties are due to the poorly measured phase differences between the ρK and $K^*\pi$ amplitudes.

C. Evidence of direct CP violation in $B^0 \rightarrow K^{*+}\pi^-$ decays

Measurements of direct CP violation are made in both the analyses of $B^0 \rightarrow K^+\pi^-\pi^0$ and $B^0 \rightarrow K_S^0\pi^+\pi^-$. Since these analyses are statistically independent, the measurements of A_{CP} may be combined for intermediate resonances common to both. The combined measurement of direct CP violation for $B^0 \rightarrow K^*(892)^+\pi^-$ decays is found to be $A_{CP}(K^{*+}\pi^-) = -0.24 \pm 0.07(\text{stat}) \pm 0.02(\text{syst})$ and is significant at 3.1σ . Likelihood scans illustrating the measurement of $A_{CP}(K^{*+}\pi^-)$ in $B^0 \rightarrow K^+\pi^-\pi^0$ and the combined result including the measurement in $B^0 \rightarrow K_S^0\pi^+\pi^-$ are shown in Fig. 14.

IX. SUMMARY

In summary, we analyze the DP distribution for $B^0 \rightarrow K^+\pi^-\pi^0$ decays from a sample of $4.54 \times 10^8 B\bar{B}$ pairs. We determine branching fractions, CP asymmetries, and

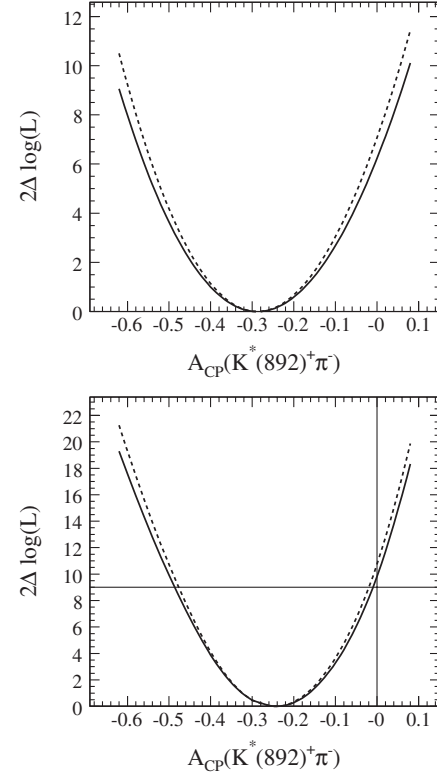


FIG. 14. Likelihood scans for $A_{CP}(K^*(892)^+\pi^-)$ using only the $B^0 \rightarrow K^+\pi^-\pi^0$ analysis (top) and the combined measurement with the $B^0 \rightarrow K_S^0\pi^+\pi^-$ analysis (bottom). The solid (dashed) line shows the $2\Delta \log(L)$ for the total (statistical) uncertainty. We measure $A_{CP}(K^{*+}\pi^-) = -0.29 \pm 0.11(\text{stat}) \pm 0.02(\text{syst})$ (Table VI) in $B^0 \rightarrow K^+\pi^-\pi^0$ and $A_{CP}(K^{*+}\pi^-) = -0.24 \pm 0.07(\text{stat}) \pm 0.02(\text{syst})$ when the measurement in $B^0 \rightarrow K_S^0\pi^+\pi^-$ is combined. The vertical line highlights $A_{CP} = 0$ and the horizontal line corresponds to $2\Delta \log \mathcal{L} = 9$, i.e. 3σ .

phase differences of seven intermediate resonances in addition to a NR contribution. We find that the isospin amplitude constructed from $B^0 \rightarrow K^*\pi$ amplitudes is consistent with 0, preventing the possibility of a useful CKM constraint as originally suggested in Ref. [3]. A similar construction made with $B^0 \rightarrow \rho K$ amplitudes provides sufficient sensitivity to measure the weak phase of the isospin amplitude. We measure $\Phi_{3/2} = -10_{-20}^{+10}(\text{stat})_{-22}^{+7}(\text{syst})^\circ$ using $B^0 \rightarrow \rho K$ amplitudes. Fundamentally, the sensitivity of $B^0 \rightarrow K^*\pi$ and $B^0 \rightarrow \rho K$ decay amplitudes to the CKM angle γ is limited by their QCD penguin dominance [28], the isospin amplitude constructed from a linear combination of such amplitudes being QCD penguin-free. We suggest that isospin combinations of $B_s \rightarrow K^*\pi$ and $B_s \rightarrow \rho K$ amplitudes, which are not QCD penguin-dominated, will provide a much more sensitive CKM constraint [29]. We also produce the first test of a CP rate asymmetry sum rule [Eq. (3)] using isospin amplitudes. We find the violation of this sum rule to be $\Sigma_{3/2} = 0.82_{-0.92}^{+0.18}(\text{stat})_{-1.35}^{+0.11}(\text{syst})$, consistent

with 0. A significant violation of the sum rule could indicate the presence of new physics operators [8], making further study of the isospin amplitudes presented in this paper an interesting area of study. Finally, we find evidence of direct CP violation in $B^0 \rightarrow K^{*+} \pi^-$ decays shown in Fig. 14, $A_{CP}(K^*(892)^+ \pi^-) = -0.24 \pm 0.07(\text{stat}) \pm 0.02(\text{syst})$, when measurements from the $B^0 \rightarrow K^+ \pi^- \pi^0$ and $B^0 \rightarrow K_S^0 \pi^+ \pi^-$ [5] DP analyses are combined.

ACKNOWLEDGMENTS

We thank Michael Gronau, Dan Pirjol, and Jonathan Rosner for useful discussions. We are grateful for the

extraordinary contributions of our PEP-II colleagues in achieving the excellent luminosity and machine conditions that have made this work possible. The success of this project also relies critically on the expertise and dedication of the computing organizations that support *BABAR*. The collaborating institutions wish to thank SLAC for its support and the kind hospitality extended to them. This work is supported by the US Department of Energy and National Science Foundation, the Natural Sciences and Engineering Research Council (Canada), the Commissariat à l'Énergie Atomique and Institut National de Physique Nucléaire et de Physique des Particules (France), the

TABLE VIII. Summary of fit results for the four solutions. The isobar parameters $\bar{a}^{(-)}$ and $\bar{\Phi}^{(-)}$ are defined in Eq. (4). The phases $\bar{\Phi}$ are measured relative to $B^0(\bar{B}^0) \rightarrow \rho(770)^{\mp} K^{\pm}$ in degrees and the $\bar{a}^{(-)}$ are measured relative to $\bar{B}^0 \rightarrow \rho(770)^+ K^-$ so that $\bar{a}_{\rho(770)^+ K^-} = 1$. The uncertainties are statistical only.

Amplitude	Parameter	Solution I	Solution II	Solution III	Solution IV
$\rho(770)^- K^+$	ΔNLL	0.00	5.43	7.04	12.33
	a	0.82 ± 0.08	0.82 ± 0.09	0.83 ± 0.07	0.84 ± 0.10
	\bar{a}	1 (fixed)	1 (fixed)	1 (fixed)	1 (fixed)
	$\bar{\Phi}$	0 (fixed)	0 (fixed)	0 (fixed)	0 (fixed)
	$\bar{\Phi}$	0 (fixed)	0 (fixed)	0 (fixed)	0 (fixed)
$\rho(1450)^- K^+$	a	0.57 ± 0.14	0.48 ± 0.26	0.59 ± 0.12	0.49 ± 0.20
	\bar{a}	0.52 ± 0.15	0.52 ± 0.16	0.54 ± 0.13	0.55 ± 0.22
	$\bar{\Phi}$	126 ± 25	90 ± 22	126 ± 25	89 ± 22
	$\bar{\Phi}$	74 ± 19	74 ± 18	72 ± 20	71 ± 21
	$\rho(1700)^- K^+$	a	0.33 ± 0.15	0.11 ± 0.31	0.34 ± 0.13
\bar{a}		0.23 ± 0.12	0.23 ± 0.12	0.17 ± 0.12	0.17 ± 0.17
$\bar{\Phi}$		50 ± 38	35 ± 164	50 ± 34	34 ± 159
$\bar{\Phi}$		18 ± 36	17 ± 35	-15 ± 48	-17 ± 57
$K^*(892)^+ \pi^-$		a	0.66 ± 0.06	0.66 ± 0.07	0.67 ± 0.05
	\bar{a}	0.49 ± 0.06	0.49 ± 0.06	0.55 ± 0.06	0.54 ± 0.08
	$\bar{\Phi}$	39 ± 25	156 ± 25	40 ± 25	156 ± 25
	$\bar{\Phi}$	33 ± 22	33 ± 22	172 ± 20	172 ± 21
	$K^*(892)^0 \pi^0$	a	0.57 ± 0.06	0.57 ± 0.06	0.58 ± 0.06
\bar{a}		0.49 ± 0.05	0.49 ± 0.05	0.50 ± 0.05	0.51 ± 0.07
$\bar{\Phi}$		17 ± 20	17 ± 21	17 ± 21	16 ± 21
$\bar{\Phi}$		29 ± 18	29 ± 18	9 ± 18	9 ± 19
$(K\pi)_0^{*+} \pi^-$		a	1.15 ± 0.09	1.22 ± 0.10	1.18 ± 0.07
	\bar{a}	1.24 ± 0.09	1.24 ± 0.09	1.32 ± 0.08	1.33 ± 0.14
	$\bar{\Phi}$	-130 ± 22	-19 ± 25	-130 ± 22	-19 ± 24
	$\bar{\Phi}$	-167 ± 16	-168 ± 16	-38 ± 18	-38 ± 19
	$(K\pi)_0^{*0} \pi^0$	a	0.91 ± 0.07	1.25 ± 0.10	0.93 ± 0.07
\bar{a}		0.78 ± 0.08	0.78 ± 0.09	1.11 ± 0.07	1.12 ± 0.11
$\bar{\Phi}$		10 ± 17	21 ± 17	10 ± 17	21 ± 17
$\bar{\Phi}$		13 ± 17	13 ± 17	1 ± 14	1 ± 14
NR		a	0.56 ± 0.08	0.31 ± 0.09	0.58 ± 0.08
	\bar{a}	0.62 ± 0.07	0.63 ± 0.07	0.57 ± 0.08	0.58 ± 0.09
	$\bar{\Phi}$	87 ± 21	-61 ± 22	87 ± 21	-61 ± 22
	$\bar{\Phi}$	48 ± 14	48 ± 14	-65 ± 15	-65 ± 17

Bundesministerium für Bildung und Forschung and Deutsche Forschungsgemeinschaft (Germany), the Istituto Nazionale di Fisica Nucleare (Italy), the Foundation for Fundamental Research on Matter (The Netherlands), the Research Council of Norway, the Ministry of Education and Science of the Russian Federation, Ministerio de Ciencia e Innovación (Spain), and the Science and Technology Facilities Council (United Kingdom). Individuals have received support from the Marie-Curie IEF program (European Union), the A.P. Sloan Foundation (USA), and the Binational Science Foundation (USA-Israel).

APPENDIX

The results of the four solutions found in the ML fit are summarized in Table VIII. Only the statistical uncertainties are quoted in this summary. The systematic uncertainties are summarized in Tables IX and X. The CP averaged interference fractions, I_{kl} , among the intermediate decay amplitudes are given in Table XI for solution I, expressed as a percentage of the total charmless decay amplitude. Here,

$$I_{kl} = \frac{|\mathcal{A}_k|^2 + |\bar{\mathcal{A}}_k|^2}{|\sum_j \mathcal{A}_j|^2 + |\sum_j \bar{\mathcal{A}}_j|^2} \quad (\text{A1})$$

for $k = l$ and

TABLE IX. Systematic uncertainties associated with the $B^0 \rightarrow K^* \pi$ isobar parameters summarized in Table VIII under solution I. Uncertainties in the phases are in degrees.

Amplitude		$\sigma(a)$	$\sigma(\bar{a})$	$\sigma(\Phi)[^\circ]$	$\sigma(\bar{\Phi})[^\circ]$
$K^*(892)^+ \pi^-$	Isobar model	0.00	0.00	16	19
	B Backgrounds	0.01	0.01	1	1
	PDF shape parameters	0.03	0.01	3	1
	SCF fraction	0.00	0.00	1	1
	PID systematics	0.00	0.00	0	1
	Line shapes	0.01	0.00	9	4
	Fit bias	0.02	0.01	6	6
	Continuum DP	0.00	0.00	2	1
	<i>Total</i>	<i>0.04</i>	<i>0.02</i>	<i>20</i>	<i>20</i>
$(K\pi)_0^{*+} \pi^-$	Isobar model	0.02	0.02	19	36
	B Backgrounds	0.01	0.01	1	1
	PDF shape parameters	0.04	0.05	3	1
	SCF fraction	0.00	0.00	1	1
	PID systematics	0.01	0.01	0	1
	Line shapes	0.01	0.01	8	3
	Fit bias	0.03	0.03	6	6
	Continuum DP	0.03	0.03	4	5
	<i>Total</i>	<i>0.06</i>	<i>0.07</i>	<i>22</i>	<i>37</i>
$K^*(892)^0 \pi^0$	Isobar model	0.02	0.01	2	0
	B Backgrounds	0.01	0.01	1	1
	PDF shape parameters	0.02	0.02	1	1
	SCF fraction	0.00	0.00	0	0
	PID systematics	0.00	0.00	1	0
	Line shapes	0.01	0.00	4	4
	Fit bias	0.01	0.00	1	1
	Continuum DP	0.01	0.01	6	5
	<i>Total</i>	<i>0.03</i>	<i>0.02</i>	<i>8</i>	<i>6</i>
$(K\pi)_0^{*0} \pi^0$	Isobar model	0.02	0.03	14	9
	B Backgrounds	0.01	0.02	1	1
	PDF shape Parameters	0.03	0.02	1	1
	SCF fraction	0.00	0.00	0	0
	PID systematics	0.00	0.01	0	0
	Line shapes	0.01	0.02	4	6
	Fit bias	0.01	0.00	1	1
	Continuum DP	0.01	0.03	6	4
	<i>Total</i>	<i>0.04</i>	<i>0.06</i>	<i>16</i>	<i>12</i>

TABLE X. Systematic uncertainties associated with the $B^0 \rightarrow \rho^- K^+$ and nonresonant isobar parameters summarized in Table VIII under solution I. Uncertainties in the phases are in degrees.

Amplitude		$\sigma(a)$	$\sigma(\bar{a})$	$\sigma(\Phi)[^\circ]$	$\sigma(\bar{\Phi})[^\circ]$
$\rho(770)^- K^+$	Isobar model	0.06	fixed	fixed	fixed
	B backgrounds	0.01	fixed	fixed	fixed
	PDF shape parameters	0.02	fixed	fixed	fixed
	SCF fraction	0.00	fixed	fixed	fixed
	PID systematics	0.01	fixed	fixed	fixed
	Line shapes	0.01	fixed	fixed	fixed
	Fit bias	0.01	fixed	fixed	fixed
	Continuum DP	0.01	fixed	fixed	fixed
	<i>Total</i>	<i>0.07</i>	<i>fixed</i>	<i>fixed</i>	<i>fixed</i>
$\rho(1450)^- K^+$	Isobar model	0.04	0.03	25	5
	B backgrounds	0.03	0.04	1	1
	PDF shape parameters	0.02	0.05	1	2
	SCF fraction	0.00	0.01	0	1
	PID systematics	0.00	0.02	1	0
	Line shapes	0.03	0.02	5	5
	Fit bias	0.02	0.01	2	4
	Continuum DP	0.00	0.02	1	3
	<i>Total</i>	<i>0.07</i>	<i>0.08</i>	<i>26</i>	<i>9</i>
$\rho(1700)^- K^+$	Isobar model	0.01	0.02	16	12
	B backgrounds	0.04	0.02	2	3
	PDF shape parameters	0.02	0.02	3	0
	SCF fraction	0.01	0.00	0	1
	PID systematics	0.00	0.01	1	0
	Line shapes	0.04	0.05	10	9
	Fit bias	0.02	0.05	4	1
	Continuum DP	0.00	0.01	0	4
	<i>Total</i>	<i>0.06</i>	<i>0.08</i>	<i>20</i>	<i>16</i>
NR	Isobar model	0.01	0.00	13	1
	B backgrounds	0.01	0.01	1	1
	SCF fraction	0.00	0.00	0	1
	PID systematics	0.00	0.01	0	1
	Line shapes	0.02	0.01	8	4
	Fit bias	0.05	0.01	1	2
	Continuum DP	0.02	0.02	1	3
	<i>Total</i>	<i>0.07</i>	<i>0.04</i>	<i>15</i>	<i>6</i>

TABLE XI. The CP averaged interference fractions, I_{kl} , among the intermediate decay amplitudes expressed as a percentage of the total charmless decay amplitude. The interference fractions are calculated using the isobar amplitudes given in Table VIII as solution I.

	$\rho(770)^- K^+$	$\rho(1450)^- K^+$	$\rho(1700)^- K^+$	$K^*(892)^+ \pi^-$	$(K\pi)_0^{*+} \pi^-$	$K^*(892)^0 \pi^0$	$(K\pi)_0^{*0} \pi^0$	NR
$\rho(770)^- K^+$	17.61	7.22	0.88	0.47	-1.49	0.50	-0.78	0.00
$\rho(1450)^- K^+$		6.34	-1.71	0.60	0.65	0.42	0.97	0.00
$\rho(1700)^- K^+$			1.68	0.22	-0.72	0.23	-0.28	0.00
$K^*(892)^+ \pi^-$				7.05	0.00	-0.05	-0.10	0.00
$(K\pi)_0^{*+} \pi^-$					30.30	-0.08	0.34	-0.08
$K^*(892)^0 \pi^0$						5.87	0.00	0.00
$(K\pi)_0^{*0} \pi^0$							15.29	1.16
NR								7.49

TABLE XII. Correlation coefficients among the floated isobar parameters for B decays.

		$(K\pi)_0^{*+} \pi^-$		$(K\pi)_0^{*0} \pi^0$		$K^*(892)^+ \pi^-$	
		a	Φ	a	Φ	a	Φ
$(K\pi)_0^{*+} \pi^-$	a	1.00	-0.07	0.65	-0.01	0.51	-0.06
	Φ	-0.07	1.00	0.17	0.56	0.03	0.94
$(K\pi)_0^{*0} \pi^0$	a	0.65	0.17	1.00	0.17	0.52	0.15
	Φ	-0.01	0.56	0.17	1.00	-0.01	0.51
$K^*(892)^+ \pi^-$	a	0.51	0.03	0.52	-0.01	1.00	0.03
	Φ	-0.06	0.94	0.15	0.51	0.03	1.00
$K^*(892)^0 \pi^0$	a	0.56	0.01	0.36	-0.04	0.42	0.00
	Φ	0.00	0.51	0.17	0.86	-0.01	0.46
NR	a	0.43	-0.38	0.15	0.02	0.37	-0.36
	Φ	0.07	0.63	0.18	0.68	-0.05	0.53
$\rho(1450)^- K^+$	a	0.31	-0.19	0.14	-0.13	0.20	-0.20
	Φ	0.06	0.52	0.11	0.58	0.04	0.46
$\rho(1700)^- K^+$	a	0.23	-0.28	0.06	-0.20	0.14	-0.27
	Φ	-0.12	0.62	0.10	0.56	-0.03	0.56
$\rho(770)^- K^+$	a	0.56	0.17	0.56	0.20	0.45	0.16

TABLE XIII. Correlation coefficients among the floated isobar parameters for B decays.

		$K^{*0}(892)\pi^0$		NR		$\rho(1450)^- K^+$		$\rho(1700)^- K^+$		$\rho(770)^- K^+$	
		a	Φ	a	Φ	a	Φ	a	Φ	a	
$(K\pi)_0^{*+} \pi^-$	a	0.56	0.00	0.43	0.07	0.31	0.06	0.23	-0.12	0.56	
	Φ	0.01	0.51	-0.38	0.63	-0.19	0.52	-0.28	0.62	0.17	
$(K\pi)_0^{*0} \pi^0$	a	0.36	0.17	0.15	0.18	0.14	0.11	0.06	0.10	0.56	
	Φ	-0.04	0.86	0.02	0.68	-0.13	0.58	-0.20	0.56	0.20	
$K^*(892)^+ \pi^-$	a	0.42	-0.01	0.37	-0.05	0.20	0.04	0.14	-0.03	0.45	
	Φ	0.00	0.46	-0.36	0.53	-0.20	0.46	-0.27	0.56	0.16	
$K^*(892)^0 \pi^0$	a	1.00	-0.09	0.25	0.09	0.27	0.18	0.24	-0.10	0.42	
	Φ	-0.09	1.00	0.00	0.65	-0.15	0.54	-0.14	0.50	0.20	
NR	a	0.25	0.00	1.00	-0.26	0.24	-0.05	0.21	-0.23	0.27	
	Φ	0.09	0.65	-0.26	1.00	-0.16	0.71	-0.22	0.63	0.24	
$\rho(1450)^- K^+$	a	0.27	-0.15	0.24	-0.16	1.00	0.02	0.70	-0.67	-0.10	
	Φ	0.18	0.54	-0.05	0.71	0.02	1.00	0.16	0.46	0.36	
$\rho(1700)^- K^+$	a	0.24	-0.14	0.21	-0.22	0.70	0.16	1.00	-0.61	-0.01	
	Φ	-0.10	0.50	-0.23	0.63	-0.67	0.46	-0.61	1.00	0.27	
$\rho(770)^- K^+$	a	0.42	0.20	0.27	0.24	-0.10	0.36	-0.01	0.27	1.00	

TABLE XIV. Correlation coefficients among the floated isobar parameters for \bar{B} decays.

		$(K\pi)_0^{*-} \pi^+$		$(K\pi)_0^{*0} \pi^0$		$K^*(892)^- \pi^+$	
		\bar{a}	$\bar{\Phi}$	\bar{a}	$\bar{\Phi}$	\bar{a}	$\bar{\Phi}$
$(K\pi)_0^{*-} \pi^+$	\bar{a}	1.00	0.09	-0.44	0.05	-0.39	0.10
	$\bar{\Phi}$	0.09	1.00	0.01	0.35	0.12	0.86
$(K\pi)_0^{*0} \pi^0$	\bar{a}	-0.44	0.01	1.00	0.47	0.34	0.02
	$\bar{\Phi}$	0.05	0.35	0.47	1.00	0.02	0.28
$K^*(892)^- \pi^+$	\bar{a}	-0.39	0.12	0.34	0.02	1.00	0.14
	$\bar{\Phi}$	0.10	0.86	0.02	0.28	0.14	1.00
$\bar{K}^*(892)^0 \pi^0$	\bar{a}	-0.49	0.01	0.24	0.03	0.31	-0.01
	$\bar{\Phi}$	0.07	0.34	0.34	0.80	-0.02	0.28
NR	\bar{a}	-0.49	-0.25	0.25	0.02	0.30	-0.23
	$\bar{\Phi}$	-0.09	0.33	-0.11	0.45	-0.08	0.18
$\rho(1450)^+ K^-$	\bar{a}	-0.63	-0.19	0.41	-0.17	0.35	-0.18
	$\bar{\Phi}$	0.02	0.48	0.02	0.50	0.02	0.37
$\rho(1700)^+ K^-$	\bar{a}	-0.37	-0.17	0.24	-0.13	0.22	-0.16
	$\bar{\Phi}$	0.30	0.49	-0.19	0.36	-0.14	0.39

TABLE XV. Correlation coefficients among the floated isobar parameters for \bar{B} decays.

	$\bar{K}^*(892)^0 \pi^0$		NR		$\rho(1450)^+ K^-$		$\rho(1700)^+ K^-$		
	\bar{a}	$\bar{\Phi}$	\bar{a}	$\bar{\Phi}$	\bar{a}	$\bar{\Phi}$	\bar{a}	$\bar{\Phi}$	
$(K\pi)_0^{*-} \pi^+$	\bar{a}	-0.49	0.07	-0.49	-0.09	-0.63	0.02	-0.37	0.30
	$\bar{\Phi}$	0.01	0.34	-0.25	0.33	-0.19	0.48	-0.17	0.49
$(K\pi)_0^{*0} \pi^0$	\bar{a}	0.24	0.34	0.25	-0.11	0.41	0.02	0.24	-0.19
	$\bar{\Phi}$	0.03	0.80	0.02	0.45	-0.17	0.50	-0.13	0.36
$K^*(892)^- \pi^+$	\bar{a}	0.31	-0.02	0.30	-0.08	0.35	0.02	0.22	-0.14
	$\bar{\Phi}$	-0.01	0.28	-0.23	0.18	-0.18	0.37	-0.16	0.39
$\bar{K}^*(892)^0 \pi^0$	\bar{a}	1.00	-0.05	0.25	0.05	0.35	0.03	0.23	-0.16
	$\bar{\Phi}$	-0.05	1.00	-0.01	0.49	-0.23	0.49	-0.18	0.35
NR	\bar{a}	0.25	-0.01	1.00	-0.05	0.31	0.01	0.23	-0.20
	$\bar{\Phi}$	0.05	0.49	-0.05	1.00	-0.21	0.57	-0.23	0.45
$\rho(1450)^+ K^-$	\bar{a}	0.35	-0.23	0.31	-0.21	1.00	-0.24	0.57	-0.72
	$\bar{\Phi}$	0.03	0.49	0.01	0.57	-0.24	1.00	0.13	0.47
$\rho(1700)^+ K^-$	\bar{a}	0.23	-0.18	0.23	-0.23	0.57	0.13	1.00	-0.49
	$\bar{\Phi}$	-0.16	0.35	-0.20	0.45	-0.72	0.47	-0.49	1.00

$$I_{kl} = \frac{\mathcal{A}_k \mathcal{A}_l^* + \mathcal{A}_k^* \mathcal{A}_l + \bar{\mathcal{A}}_k \bar{\mathcal{A}}_l^* + \bar{\mathcal{A}}_k^* \bar{\mathcal{A}}_l}{|\sum_j \mathcal{A}_j|^2 + |\sum_j \bar{\mathcal{A}}_j|^2} \quad (\text{A2})$$

for $k \neq l$. The \mathcal{A}_k are the amplitudes defined in Eq. (4).

The full correlation matrix for solution I is given in Tables XII, XIII, XIV, and XV. The tables are separated by correlations among B and \bar{B} decay amplitudes.

- [1] N. Cabibbo, *Phys. Rev. Lett.* **10**, 531 (1963).
[2] M. Kobayashi and T. Maskawa, *Prog. Theor. Phys.* **49**, 652 (1973).
[3] M. Ciuchini, M. Pierini, and L. Silvestrini, *Phys. Rev. D* **74**, 051301(R) (2006).
[4] M. Gronau, D. Pirjol, A. Soni, and J. Zupan, *Phys. Rev. D* **75**, 014002 (2007).
[5] B. Aubert *et al.* (BABAR Collaboration), *Phys. Rev. D* **80**, 112001 (2009).
[6] A. Wagner, Report No. SLAC-R-942, 2010 (unpublished).
[7] M. Antonelli *et al.*, *Phys. Rep.* **494**, 197 (2010).
[8] M. Gronau, D. Pirjol, and J. Zupan, *Phys. Rev. D* **81**, 094011 (2010).
[9] B. Aubert *et al.* (BABAR Collaboration), *Phys. Rev. D* **78**, 052005 (2008).
[10] B. Aubert *et al.* (BABAR Collaboration), *Phys. Rev. D* **72**, 072003 (2005).
[11] J. Blatt and V. E. Weisskopf, *Theoretical Nuclear Physics* (John Wiley & Sons, New York, 1952).
[12] C. Zemach, *Phys. Rev.* **133**, B1201 (1964).
[13] G. J. Gounaris and J. J. Sakurai, *Phys. Rev. Lett.* **21**, 244 (1968).
[14] B. Aubert *et al.* (BABAR Collaboration), *Phys. Rev. D* **76**, 012004 (2007).
[15] R. R. Akhmetshin *et al.* (CDM-2 Collaboration), *Phys. Lett. B* **527**, 161 (2002).
[16] S. Schael *et al.* (ALEPH Collaboration), *Phys. Rep.* **421**, 191 (2005).
[17] P. Estabrooks, *Phys. Rev. D* **19**, 2678 (1979).
[18] D. Aston *et al.* (LASS Collaboration), *Nucl. Phys.* **B296**, 493 (1988).
[19] C. Amsler *et al.* (Particle Data Group), *Phys. Lett. B* **667**, 1 (2008).
[20] B. Aubert *et al.* (BABAR Collaboration), *Nucl. Instrum. Methods Phys. Res., Sect. A* **479**, 1 (2002).
[21] S. Agostinelli *et al.* (GEANT4 Collaboration), *Nucl. Instrum. Methods Phys. Res., Sect. A* **506**, 250 (2003).
[22] B. Denby and D. Perret-Gallix, in *Proceedings of the Fourth International Workshop on Software Engineering, Artificial Intelligence, and Expert Systems for High Energy and Nuclear Physics, Pisa, Italy, 1995* (World Scientific, Singapore, 1995).
[23] D. Asner *et al.* (Heavy Flavor Averaging Group), [arXiv:1010.1589](https://arxiv.org/abs/1010.1589).
[24] B. Aubert *et al.* (BABAR Collaboration), *Phys. Rev. Lett.* **94**, 161803 (2005).
[25] K. S. Cranmer, *Comput. Phys. Commun.* **136**, 198 (2001).
[26] H. Albrecht *et al.*, *Z. Phys. C* **48**, 543 (1990).
[27] B. Aubert *et al.* (BABAR Collaboration), *Phys. Rev. Lett.* **91**, 201802 (2003).
[28] M. Gronau, D. Pirjol, and J. Rosner, *Phys. Rev. D* **81**, 094026 (2010).
[29] M. Ciuchini, M. Pierini, and L. Silvestrini, *Phys. Lett. B* **645**, 201 (2007).